Chapter 5

Results and Discussion

5.1 Introduction

With the deployment of temporary three-component seismic stations in the DST region, teleseismic P-to-S converted waves have been studied to map the crustal thickness and other discontinuities in the crust. The upper mantle 410 km and 660 km discontinuities have also been investigated.

5.2 Data Examples of some Individual Stations

The receiver functions for six seismic stations are plotted in Figs. 5.1 and 5.2 in a time window between -10 to 30 s, in which the direct conversions from Moho and the crustal multiples are clearly visible. The data for the other stations are analysed in a same way. The abscissa represents the conversion time for Ps with respect to the direct P-arrival time, commonly termed as 'delay time'. Fig. 5.1 shows data for the stations JS07, JW09, JW05 and JK02 located on the eastern side of the DST (see Fig. 4.1 for location). Phases are identified in the traces and marked in the summation traces of each seismic station.

For the stations JW05, JK02, ID06 and ID08 there is a clear strong and coherent phase around 1 s (Figs. 5.1-5.2), which is attributed to a thick sedimentary layer corroborated with other geophysical and geological studies in this area. However this phase is absent in the stations JS07 and JW09 as these stations are situated directly on the Precambrian crystalline basement .

The second prominent , coherent phase around 4 s, observed in all the stations is the converted phase from the Moho. The crustal multiples generated between the Moho and the free surface arrive around 14 s delay time.

An additional phase is observed between the Moho conversion and the Moho multiples, labeled as LCM (Figs. 5.1-5.2). The timing of this multiple is less than the timings of Moho multiple, hence this phase must be a multiple of lower crustal origin caused by a discontinuity in the lower crust. Also LCM is seen on the eastern side of DST and is absent on the western side. The details of the modeling results of these phases are given in the section 5.5 of this chapter.

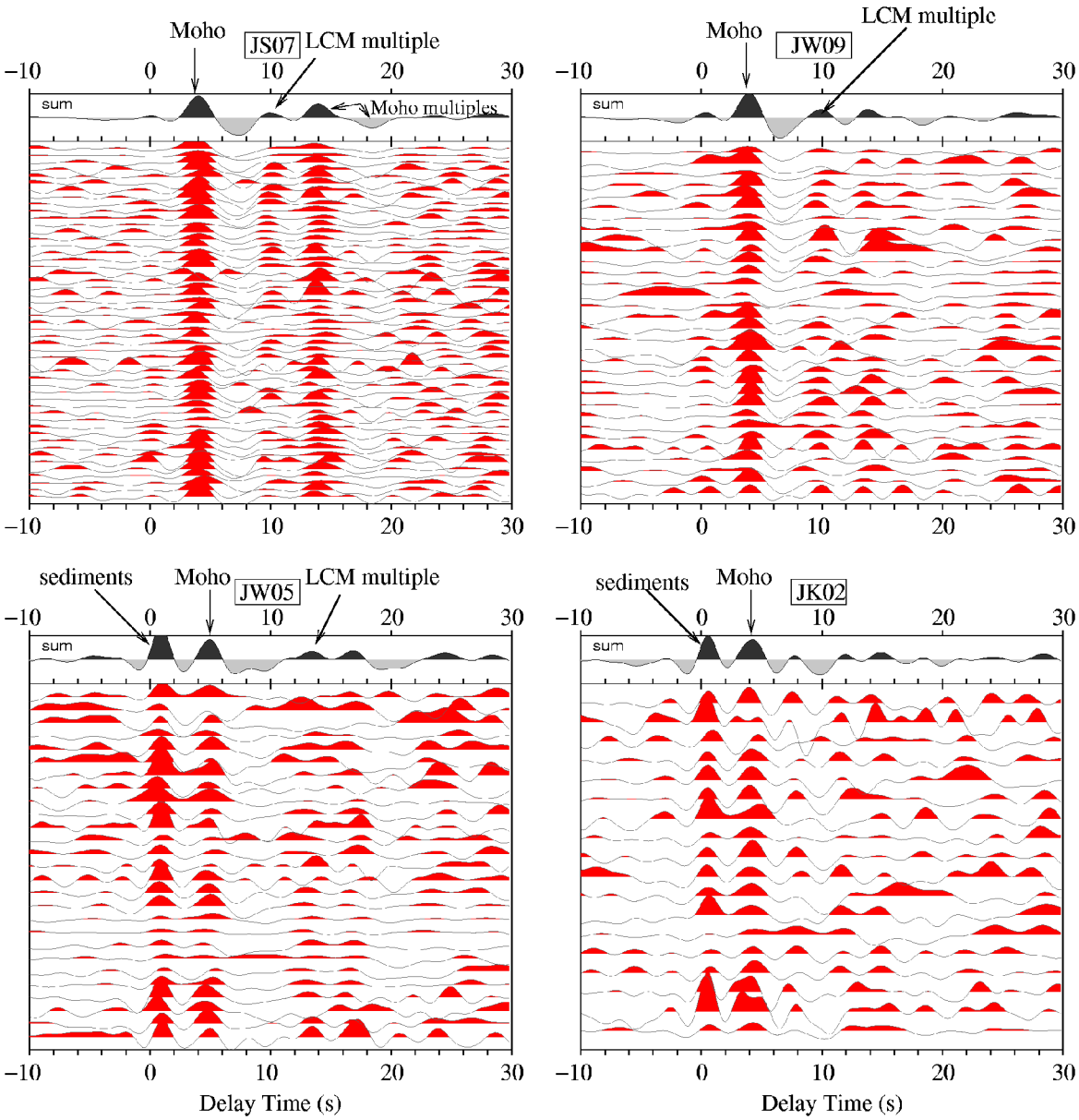

Figure (5.1): Receiver functions for the stations JS07, JW09, JW05 and JK02 situated on the eastern side of the DST (see Fig. 4.1 for the location). The abscissa denotes the delay time with respect to the P-onset time. The upper panel in each figure represents the summation trace of the receiver functions.

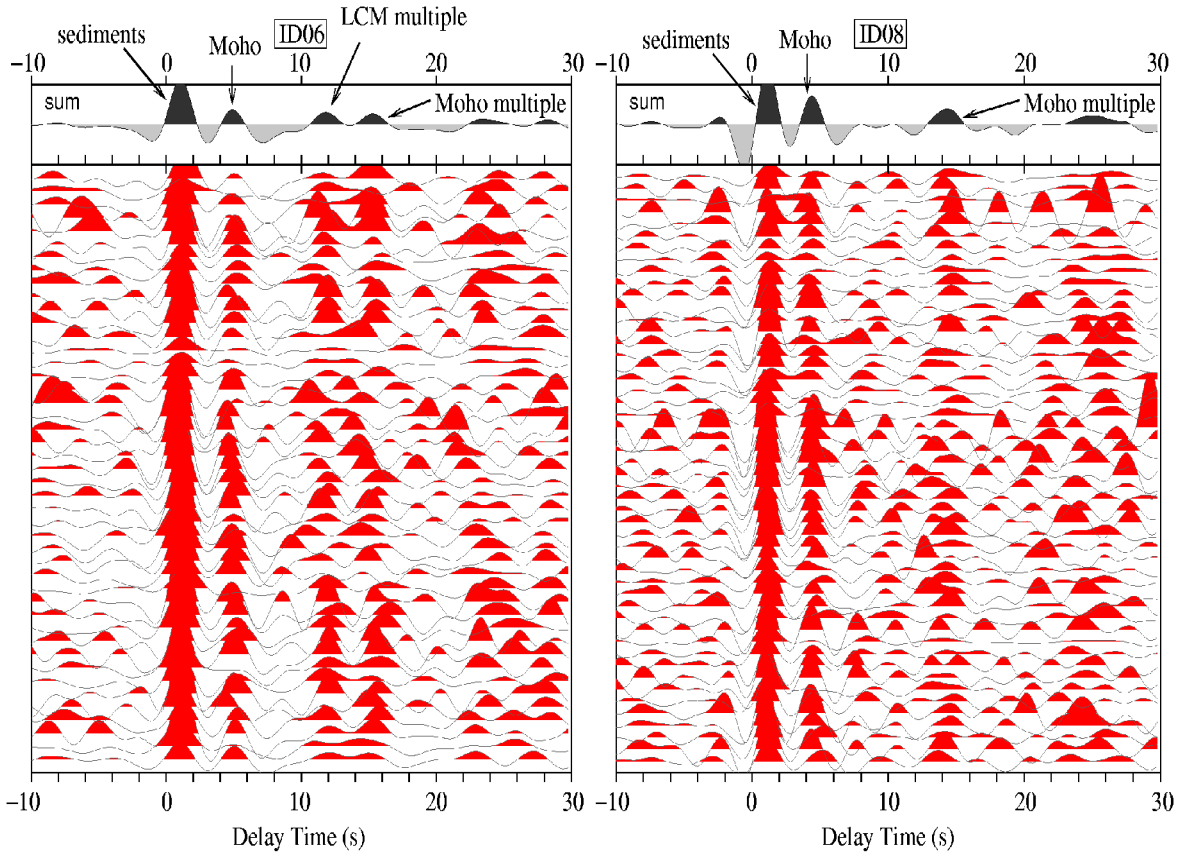

Figure (5.2): Same as Fig 5.1 for the stations ID08 and ID06 (see Fig. 4.1 for the location). Station ID06 is situated on the DST while the station ID08 is situated on the western side the DST.

5.3 Seismic Image from Receiver Function Analysis

The receiver functions for all stations of DESERT project were computed as discussed in the earlier chapter. All the receiver functions from each station are displayed according to their longitude from west to east (Fig. 5.3) . The moveout corrections have been applied with respect to IASP91 global reference model (Kennett and Engdahl, 1991) to align the phases. After moveout correction all P-to-S converted phases from any horizontal discontinuity will be parallel to that of the direct P -wave onset. The top panel shows the summation trace of all receiver functions along a vertical line.

Fig. 5.3 indicates that the receiver functions vary from station to station due to the heterogeinity from west to east. The figure shows strong differences but also show clearly the following main features :

1. A strong conversion at about 1 s delay time is observed and is present all along the transect from west to east. This strong phase is corroborated with the sediments present in that area.

2. A prominent positive P-to-S converted arrival from Moho at 4-5 s is present all along and gradually the amplitude increases from west to east.

3. Following the Moho conversion a strong negative phase at about 6-7 s is present.

4. A clear positive peak and a negative trough at about 14 s and 18 s are due to multiples from the Moho boundary and the free surface.

5. Another interesting feature around 10 s (marked by a blue ellipse) parallel to the Moho multiple is a coherent and strong phase, which we have interpreted as a multiple of lower crustal origin. This phase is only seen in the composite plot but not resolable in the summation trace due to the large wavelength of the summation trace. This phase is present only on the eastern side of the Araba fault but absent on the western side indicating that the Araba fault is of deep seated nature.

In the deeper part, there are two other phases which are brought out clearly in the summation trace , the 410 km and the 660 km global discountinuites. The thin lines at 44 s and 68 s are the above two discountinuities, have derived from the standard IASP91 global earth model. Our studies reveal that these two global discountinuities have later arrival times than the predicted ones. These discrepancy can be interpreted as the crust and upper mantle above 410 km is slower in seismic velocities than the normal crust and upper mantle in global average. The implications have been discussed in section 5.7 in detail.

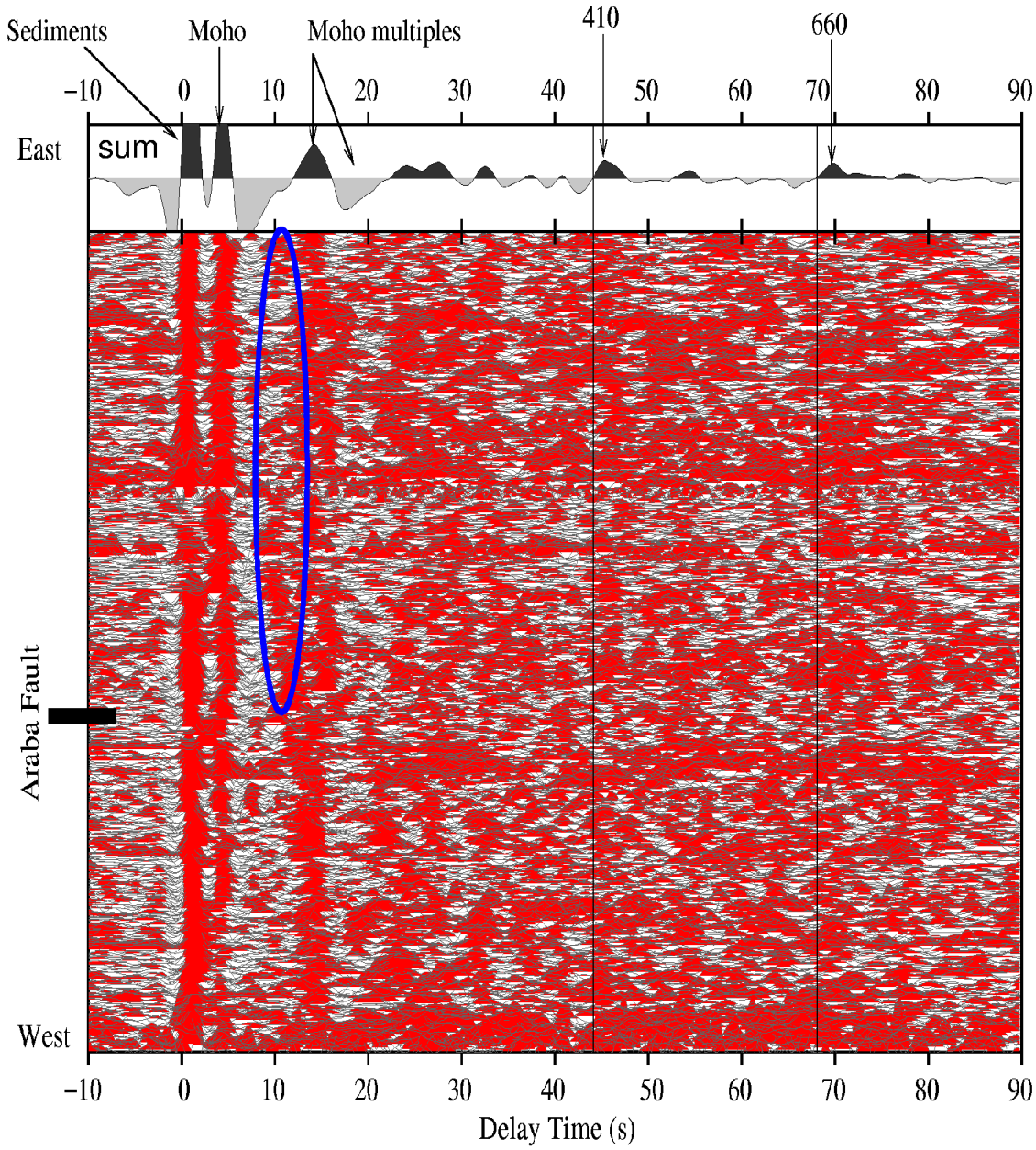

Figure (5.3): Plot of all receiver functions of DESERT temporary network. The traces are moveout-corrected for Ps conversions underneath the stations, and ordered according to their longitude (from west to east). Several crustal and upper mantle phases can be seen especially in the summation trace. The lines marked 410 and 660 are Ps converted phases calculated with the IASP91 global reference model. The blue ellipse represents additional signals rising from Araba fault towards the east and arrive parallel to the Moho multiple (see Fig. 5.4).

5.4 Moho Depth and Vp/Vs Determination

Fig. 5.4 displays 30 s of summed receiver functions for all temporary seismic stations (see Fig. 5.5 for location of stations and of piercing points at 33 km depth). On the receiver functions in Fig. 5.4 several phases are identified. The first conversion labeled 'sediments' is from within the crust. The second conversion labeled 'Moho' is the conversion from the crust-mantle boundary. In addition to the direct conversions from the sediments and the crust-mantle boundary, crustal multiples labeled 'Moho multiples' are identified.

The records in Fig. 5.4 are grouped according to the appearance of their multiples. Group A has one clear Moho multiples (PpPs), which has two additional legs in the crust. Group B has the same Moho multiple plus an additional multiple parallel to the Moho multiple, which is very likely caused by a discontinuity in the lower crust (see section 5.5 for more details). The last group, group C, has no coherent visible multiples. The spatial distribution of the members of the three groups is shown in Fig. 5.5.

Group A has with one exception (JS02), only stations east of the DST, whereas group B, again with one exception (ID16), only has stations on the DST and to the eastern part of it. In Fig. 5.4 data indicate that the internal structure of the crust varies from simple on the western side of the DST to quite complex on the eastern side.

Crustal multiples have been used to determine the crustal thickness (H) and the Vp/Vs ratio. Identifying the Moho Ps, the crustal multiples and measuring their arrival times on a single receiver function trace can be difficult due to noise. Multiple events were used by summing their receiver functions to increase the signal/noise ratio. This stacking technique is done in time domain for a cluster of events in which large amounts of teleseismic waveforms can be processed.

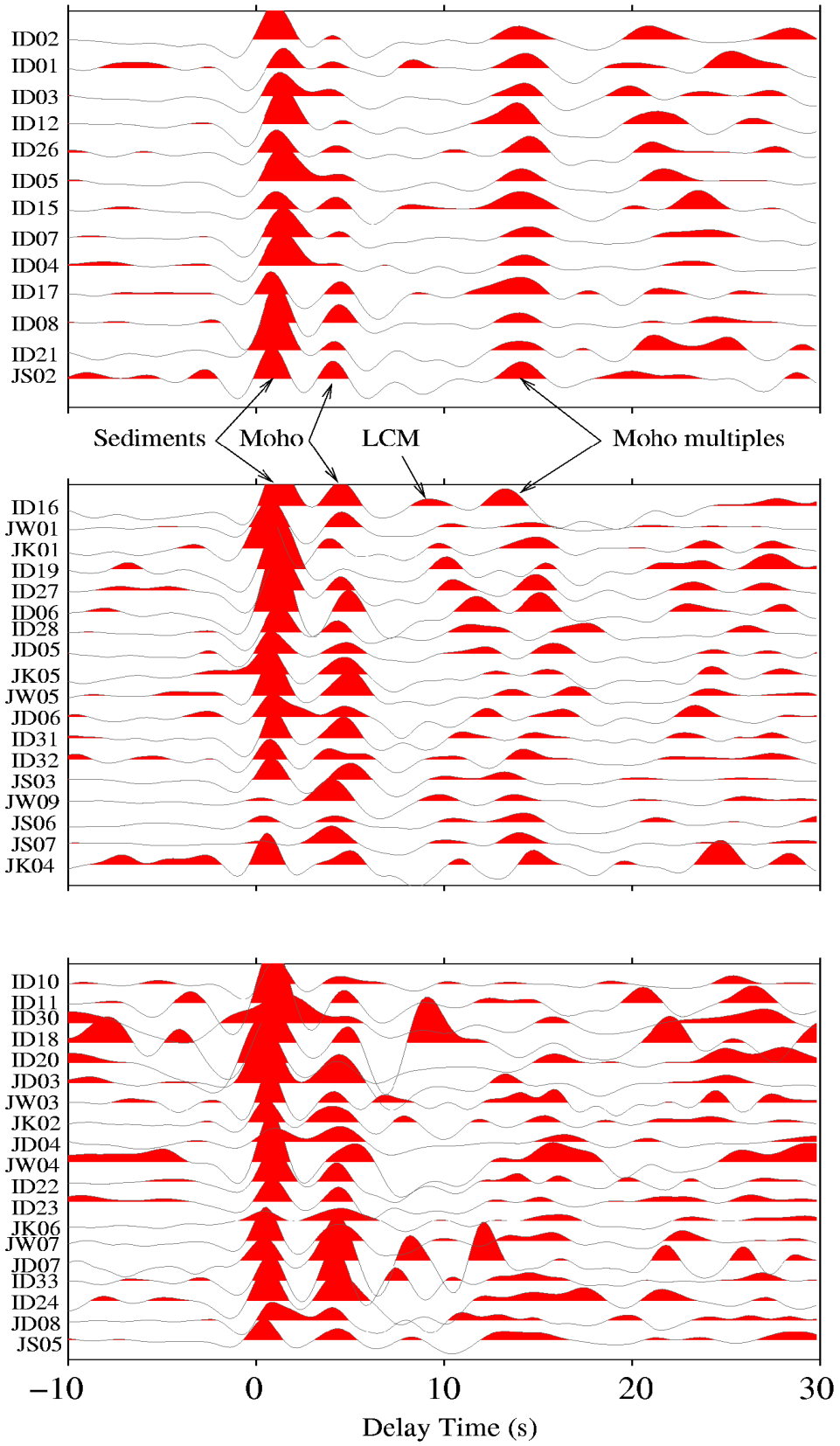

Figure (5.4): Summed receiver functions for each station. Stations are grouped according to the appearance of their multiples.

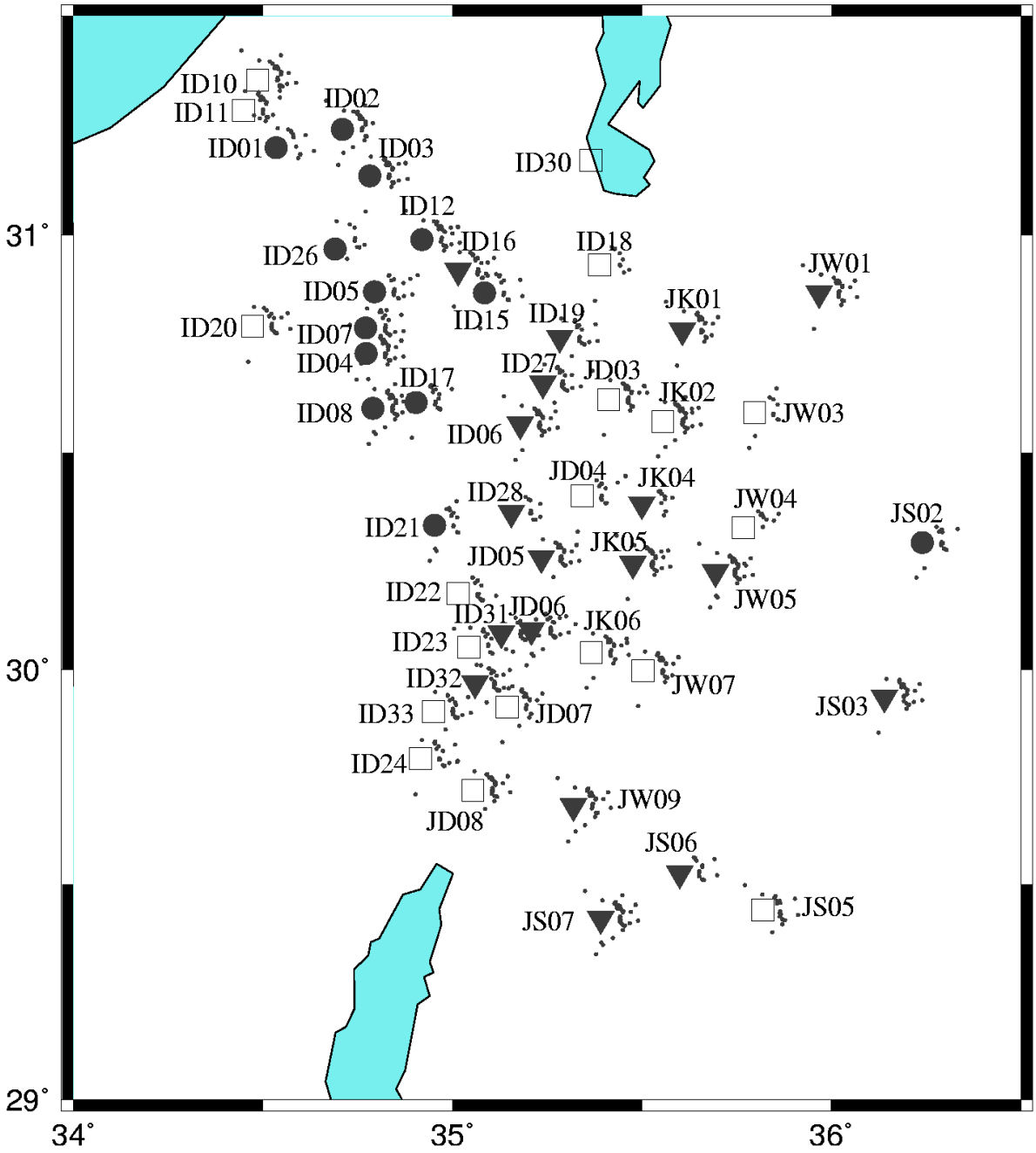

Figure (5.5): Distribution of stations of the three groups defined in Fig. 5.4. Group A: full circles, Group B: full triangles, and Group C: open squares. Piercing points at 33 km depth are also shown (small dots).

Two methods were used to determine the crustal thickness (H) and the Vp/Vs ratio. First, Zhu and Kanamori (2000) method has been used. This method performs a grid search through the H and Vp/Vs space and searches for the largest summed amplitudes at the predicted time of direct conversions and multiples, as discussed in section 2.2.6. There is no need to pick arrival times of different conversion phases. In fact both crustal thickness (H) and Vp/Vs values are the output of the method. Examples of successful application of the Zhu and Kanamori method to receiver functions are presented in Figs. 5.6 to 5.11.

The second approach was to measure visually the times of the Moho Ps conversions and the PpPs multiples to estimate the crustal thickness and the Vp/Vs ratio (equations 3.3, 3.4, 3.8) as discussed in Chapter 3. For each station the travel times for both the Moho and the Moho multiples are manually selected. Observed delay times were picked carefully at the highest amplitude of the phase which in most cases coincided with the symmetrical center of the phase. The travel times for the Moho and the Moho multiples are listed in Table 3.1, Appendix C .

The result of visual readings of delay times for all DESERT seismic stations is presented in Fig. 5.12 . It shows a clear increase of Moho delay times from west to east along the WRR profile. Most values are located in the range of 4-4.5 s delay time.

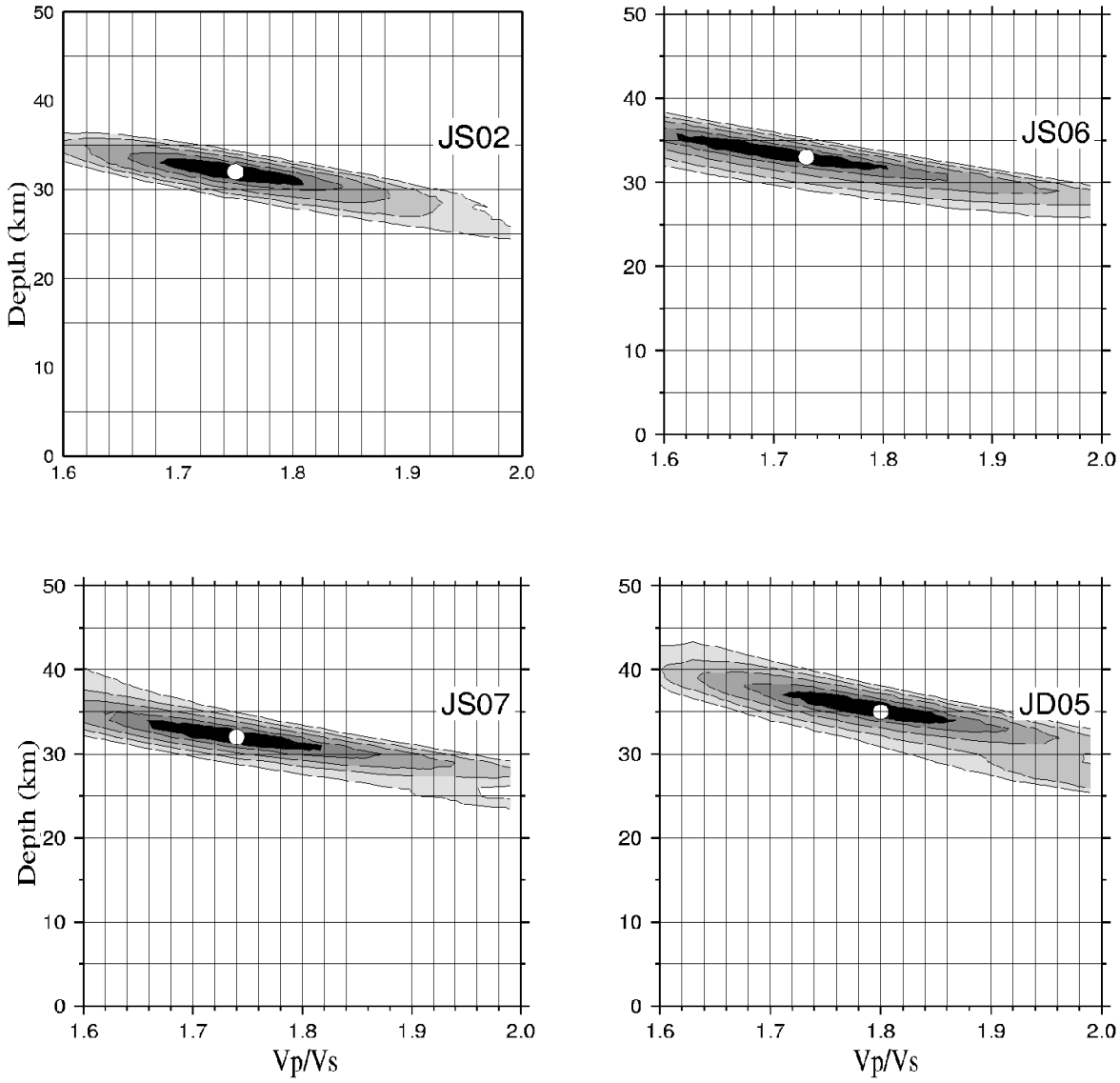

Figure (5.6): Examples of successful application of the Zhu and Kanamori (2000) method to receiver functions from stations JS02, JS06, JS07 and JD05. In fact both crustal thickness (km) and Vp/Vs values are the output of the Zhu and Kanamori mothod.

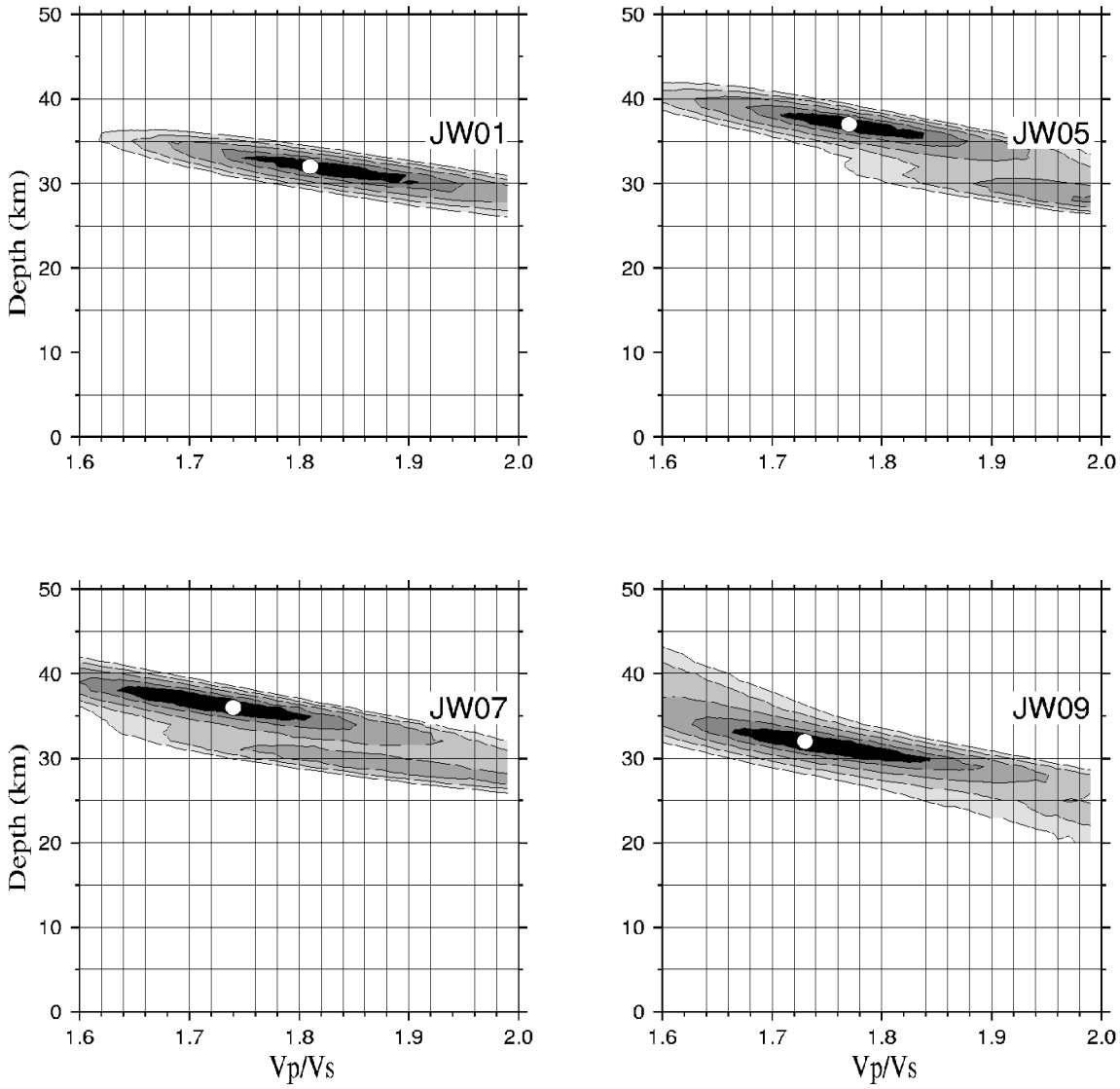

Figure (5.7): Examples of successful application of the Zhu and Kanamori (2000) method to receiver functions from stations JW01, JW05, JW07 and JW09.

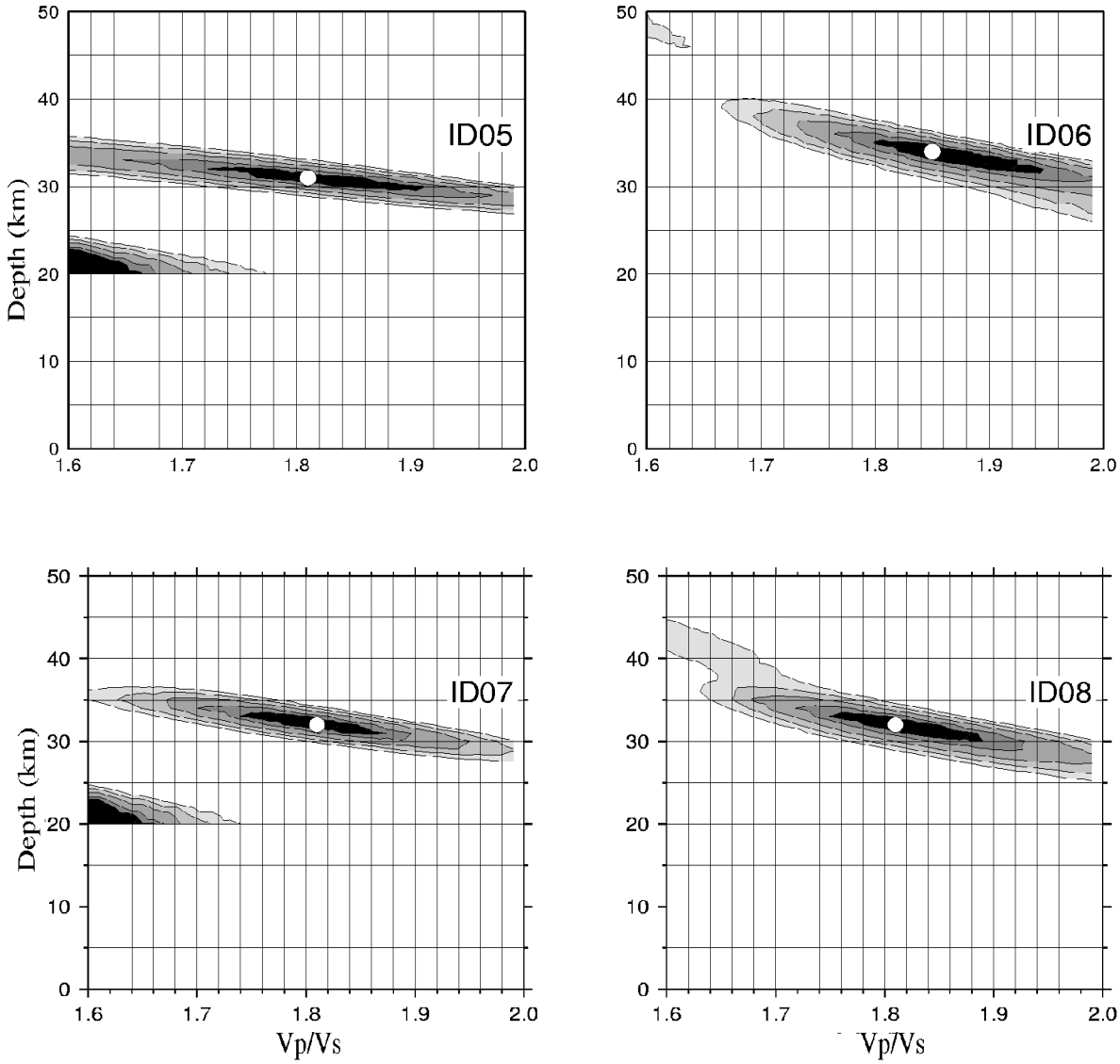

Figure (5.8): Examples of successful application of the Zhu and Kanamori (2000) method to receiver functions from stations ID05, ID06, ID07 and ID08.

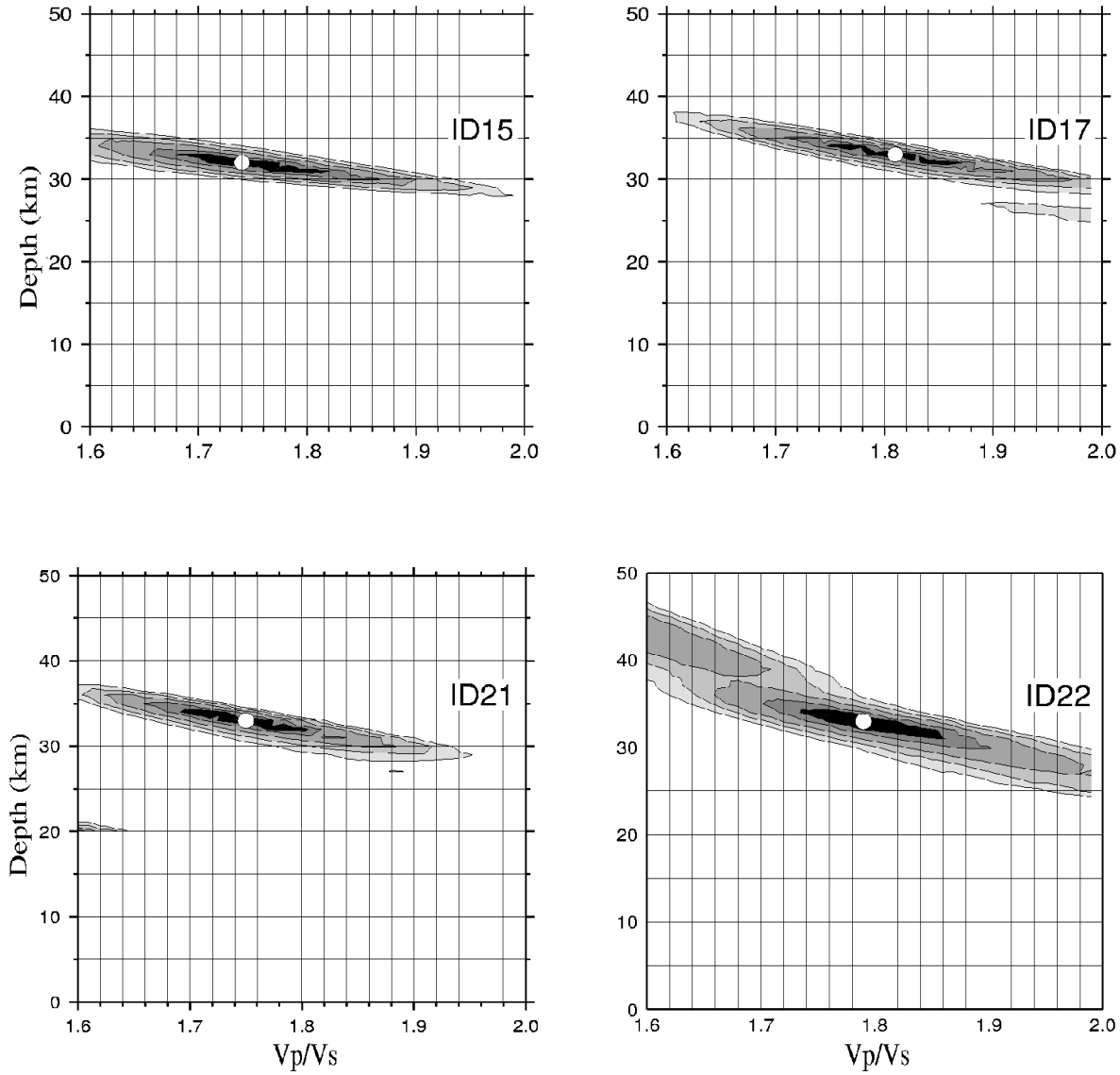

Figure (5.9): Examples of successful application of the Zhu and Kanamori (2000) method to receiver functions from stations ID15, ID17, ID21 and ID22.

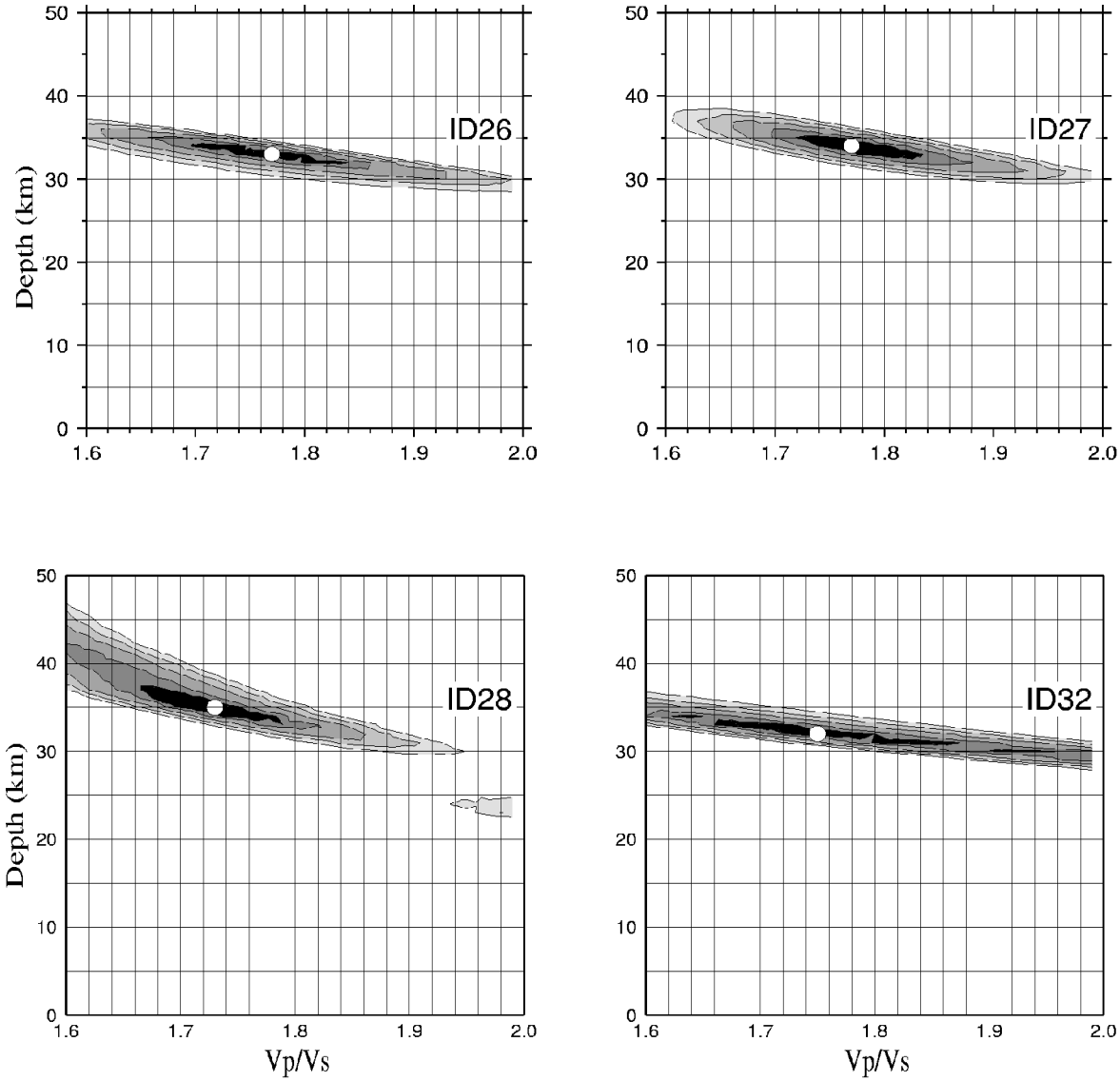

Figure (5.10): Examples of successful application of the Zhu and Kanamori (2000) method to receiver functions from stations ID26, ID27, ID28 and ID32.

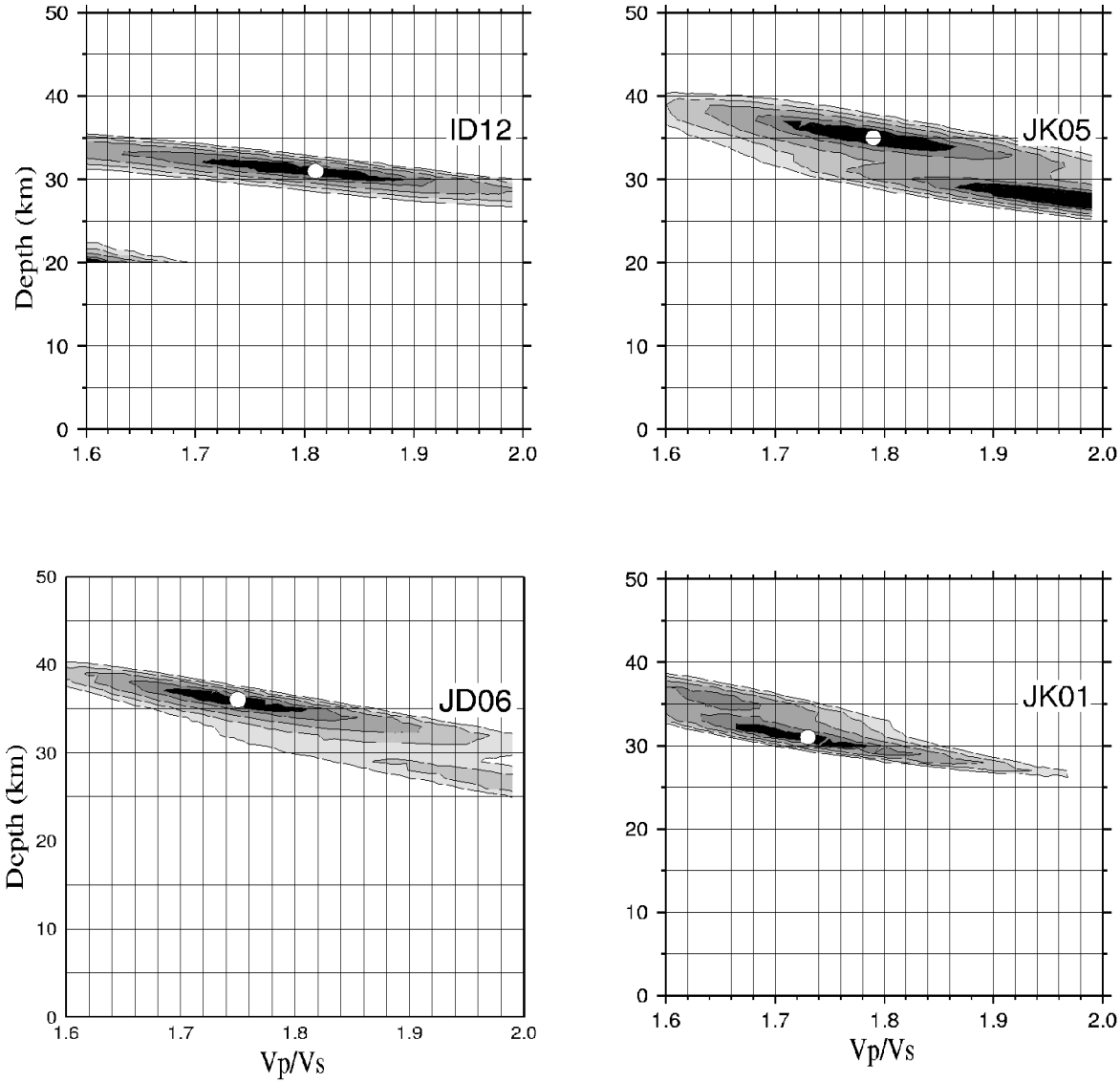

Figure (5.11): Examples of successful application of the Zhu and Kanamori (2000) method to receiver functions from stations ID12, JK05, JD06 and JK01.

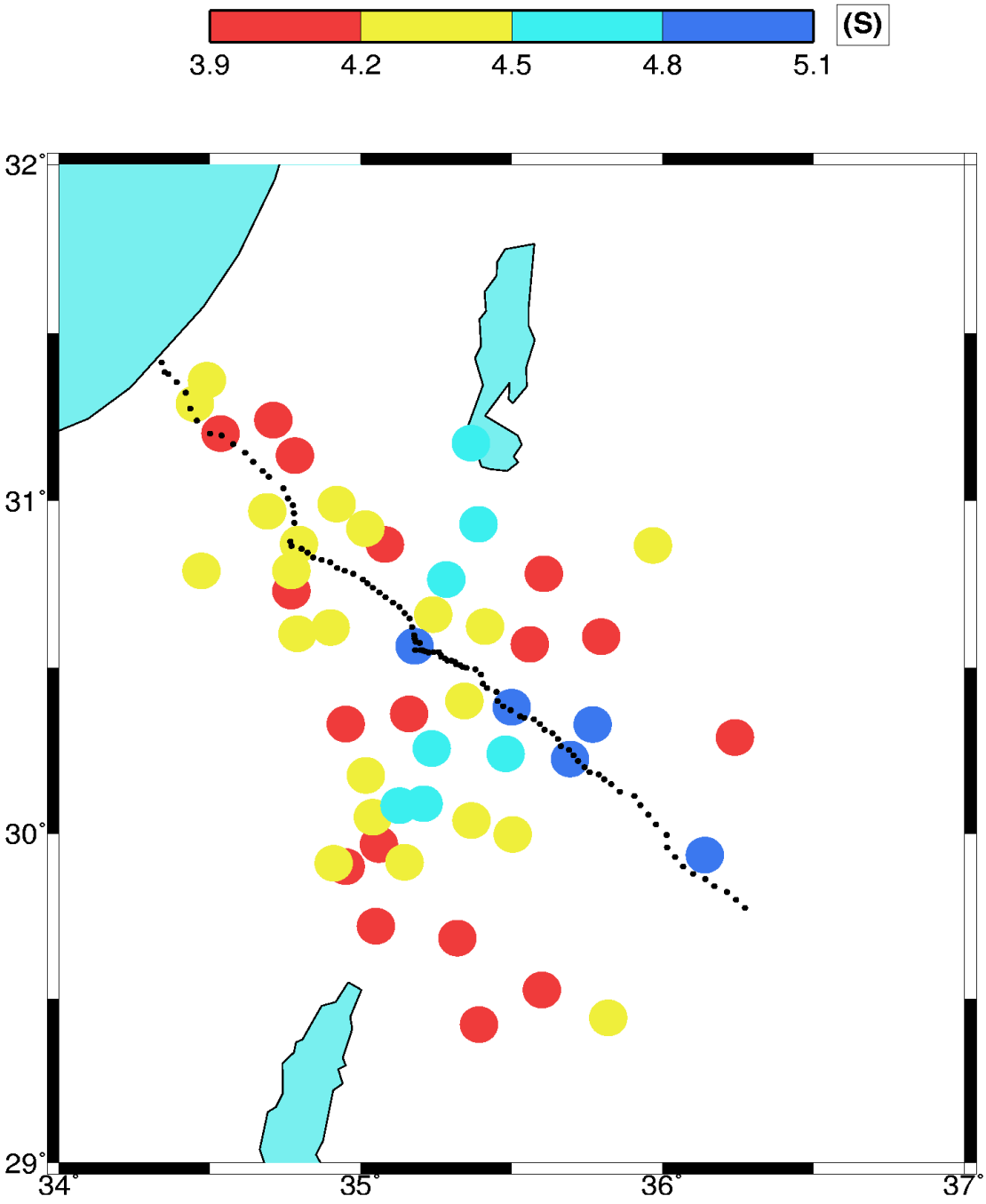

Figure (5.12): The results of visual readings of the Moho conversion phases for all DESERT seismic stations. It shows a clear increase of Moho delay times from west to east along the controlled source line. Most values are located in the range of 4-4.5 s delay time.

Table 5.1 lists the H and Vp/Vs values of each technique and their differences. In both methods, the average P velocity of the crust was fixed to 6.1 km/s. However H and Vp/Vs determinations are not very sensitive to Vp variations (Zhu and Kanamori, 2000). At group C only the Zhu and Kanamori method was applicable.

At 15 stations the difference in H is zero, at 14 stations it is 1km, and at 2 stations 2 km. The crustal Vp/Vs ratio ranges from 1.73 to 1.83 with an average of 1.77. The difference in the Vp/Vs ratio is at 27 stations less than or equal to 0.03, and at one station it is 0.40, and at 3 stations it is between 0.05 and 0.17. If the Vp/Vs ratio was smaller than 1.71 or larger than 1.85, the average crustal Vp/Vs ratio of 1.77 was used instead (at 2 stations of group B and 11 stations of group C. (see Table 5.1).

Figure 5.13 shows the resulting Moho depths H versus the Vp/Vs ratios from Table 5.1 , using the Zhu and Kanamori technique, including the corrected values marked by a star in Table 5.1. The average P velocity of the crust was fixed to 6.1km/s. A number of H-Vp/Vs pairs are double and thus Fig. 5.13 has fewer values than Table 5.1.

In both methods we need to fix the average P velocity of the crust. However, H and Vp/Vs determinations are not very sensitive to Vp variations (Zhu and Kanamori, 2000).

In Fig. 13, we have used Vp values of 6.0 and 6.2 km/s to estimate the possible errors incured in H and Vp/Vs. The crustal thickness H changes by about 0.6 km and the Vp/Vs is changed by less than 0.01 if Vp is changed by 0.1km/s. These values are shown in Fig. 5.13 for one station, but for other pairs of H-Vp/Vs the values fall in the same range. The absolute errors of the Moho depth are close to ± 1 km, and 0.01-0.03 for the average crustal Vp/Vs ratio.

Group **A**

ID	*VP/Vs (TT)*	*Vp/Vs (ZK)*	*Dif*	*H TT (km)*	*H ZK (km)*	*Dif*
ID02	1.74	1.74	0.00	31	32	1
ID01	1.75	1.74	0.01	31	31	0
ID03	1.72	1.73	0.01	32	31	1
ID12	1.85	1.83	0.02	32	31	1
ID26	1.76	1.77	0.01	33	33	0
ID05	1.81	1.81	0.00	32	31	1
ID15	1.76	1.75	0.01	32	32	0
ID07	1.80	1.81	0.01	32	32	0
ID04	1.77	1.75	0.02	32	32	0
ID17	1.80	1.81	0.01	32	33	1
ID08	1.80	1.80	0.00	33	32	1
ID21	1.77	1.75	0.02	32	33	1
JS02	1.73	1.75	0.02	33	32	1

Group **B**

ID	*VP/Vs (TT)*	*Vp/Vs (ZK)*	*Dif*	*H TT (km)*	*H ZK (km)*	*Dif*	*LCD (km)*
ID16	1.92	1.83	0.09	33	31	2	21
JW01	1.79	1.81	0.02	33	32	1	23
JK01	1.68	1.73	0.05	31	31	0	22
ID19	1.77	1.76	0.01	34	35	1	23
ID27	1.77	1.76	0.01	34	34	0	24
ID06	1.83	1.83	0.01	33	34	1	26
ID28	1.57	1.74	0.17	32	34	2	25
JK04	1.90	1.89* 1.77	0.01	34	35	1	25
JD05	1.77	1.80	0.03	34	35	1	27
JK05	1.76	1.79	0.03	35	35	0	28
JW05	1.76	1.76	0.00	37	37	0	29
JD06	1.76	1.75	0.01	36	36	1	27
ID31	1.78	1.79	0.01	33	33	0	25
ID32	1.72	1.75	0.03	32	32	0	23
JS03	2.10	1.70* 1.77	0.40	38	38	0	23
JW09	1.75	1.73	0.02	32	32	0	22
JS06	1.74	1.73	0.01	33	33	0	24
JS07	1.74	1.74	0.00	32	32	0	23

Group **C**

ID	*Vp/Vs (ZK)*		*H ZK (km)*
JD03	1.79		32
JK02	1.67*	1.77	33
JD04	1.82		34
JW04	1.93*	1.77	36
ID22	1.79		33
ID23	1.75		34
JK06	1.70*	1.77	35
JW07	1.74		35
ID33	1.73		33
ID24	1.73		33
JD08	1.62*	1.77	33
JS05	1.77		33
ID10	1.66*	1.77	30
ID11	1.60*	1.77	30
ID18	1.68*	1.77	34
ID20	1.60*	1.77	33
ID30	1.67*	1.77	33
JD07	1.69*	1.77	33
JW03	1.63*	1.77	32

Table (5.1): Comparison of determinations of the Moho depth and average Vp/Vs ratio by the Zhu and Kanamori (2000) method (ZK) and by direct time readings of direct conversions and crustal multiples (TT) for the groups A, B and C. The depth of the Lower Crustal Discontinuity (LCD) is presented in panel B.

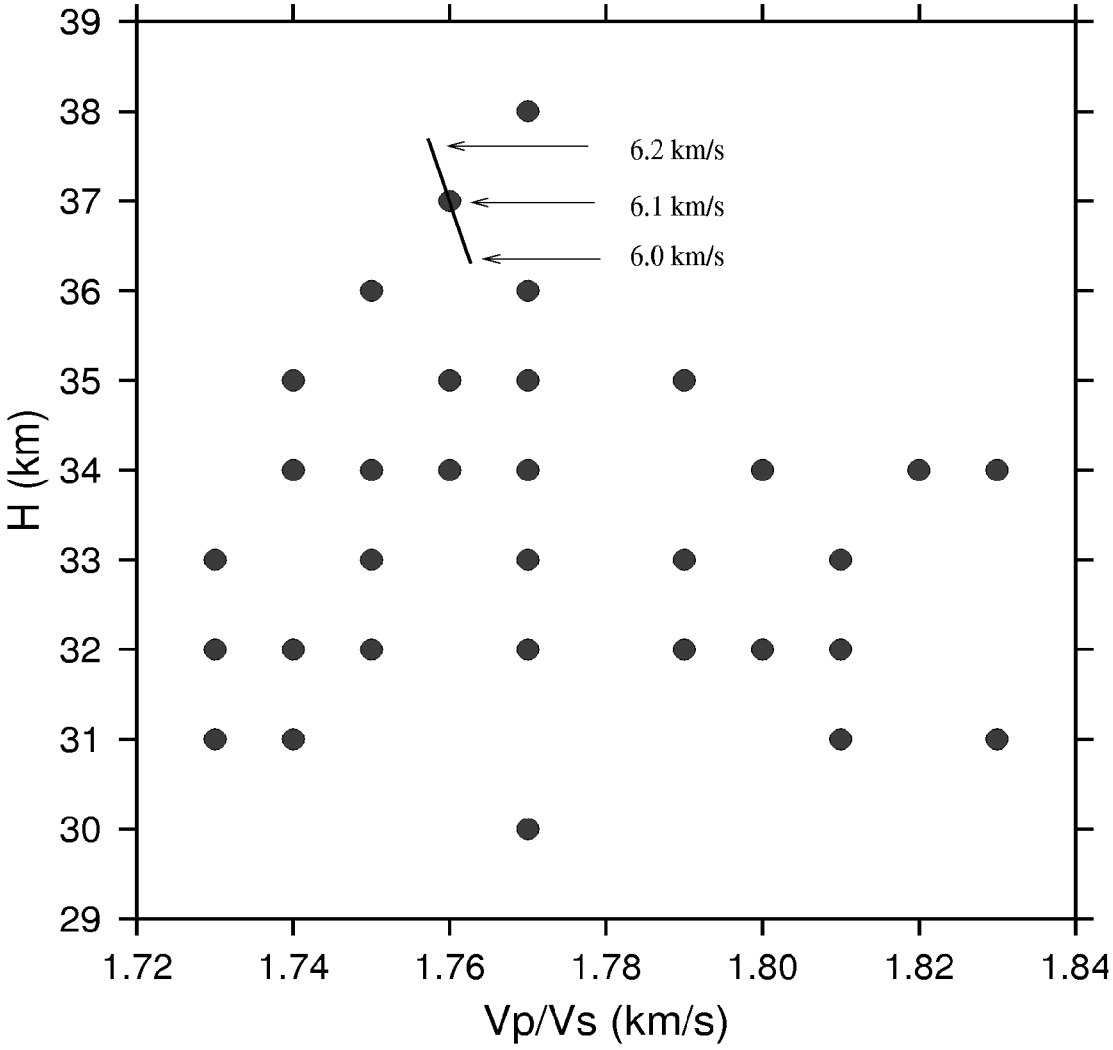

Figure (5.13): Moho depth versus Vp/Vs ratio determined from the direct Moho conversions and their multiples using the Zhu and Kanamori method and using an average crustal Vp of 6.1 km/s. Shifts of H and Vp/Vs depending on different Vp values are also indicated at one station. It shows that the Vp/Vs ratios seem to form in two groups with one group having values smaller than 1.77 and the other having values larger than 1.77. Moho depths larger than 34km seem to have Vp/Vs ratios close to about 1.76, and extremely large Vp/Vs ratios are not observed at large Moho depths.

The resulting Moho depths and Vp/Vs ratios from Table 5.1 are shown in Figs. 5.14 and 5.15, respectively, using the Zhu and Kanamori technique. The obtained Moho depths range from 30 to 38 km.

The Moho depth is larger than 34 km at 10 seismic stations. These stations are all located on the DST or to the eastern side of it (blue colors in Fig. 5.14). East of the DST, Moho depths are greatest beneath the central portion of the network and shallow towards the northern and southern ends of the network. This indicates that the Moho east of the DST forms a trough-like feature with the deepest parts exactly where the wide angle reflection/refraction profile is located (dotted line in Fig. 5.14). The existence of many faults on the eastern part of the DST that vary in size and direction might explain the lateral variations in Moho depths.

Fig. 5.16 is a projection of the Moho depths on and east of the DST onto a south-west to north-east profile perpendicular to the WRR profile. Hence the Moho depths are unusually deep at the location of the WRR profile while to the west of the DST the crust is shallower and reaches up to 33 km. In section 5.6 the crustal structure has been discussed in light of other geophysical studies in this area.

The receiver function results reveal a Moho depth that is smoothly increasing across the DST along the WRR profile. For comparison with other geophysical experiments see Section 5.7.

The distribution of the Vp/Vs values have been shown Fig. 5.15. It shows that most values are within the range of 1.73 to 1.77. There is no clear systematics in the distribution of the Vp/Vs ratios, however, from Fig. 5.13 it is seen that the Vp/Vs ratios seem to be assembled in two groups: smaller than 1.76 and larger than 1.79. The highest Vp/Vs ratios are observed somewhat west of the DST. Moho depths larger than 34 km seem to have Vp/Vs ratios close to about 1.76. Extremely large Vp/Vs ratios are not observed at large Moho depths.

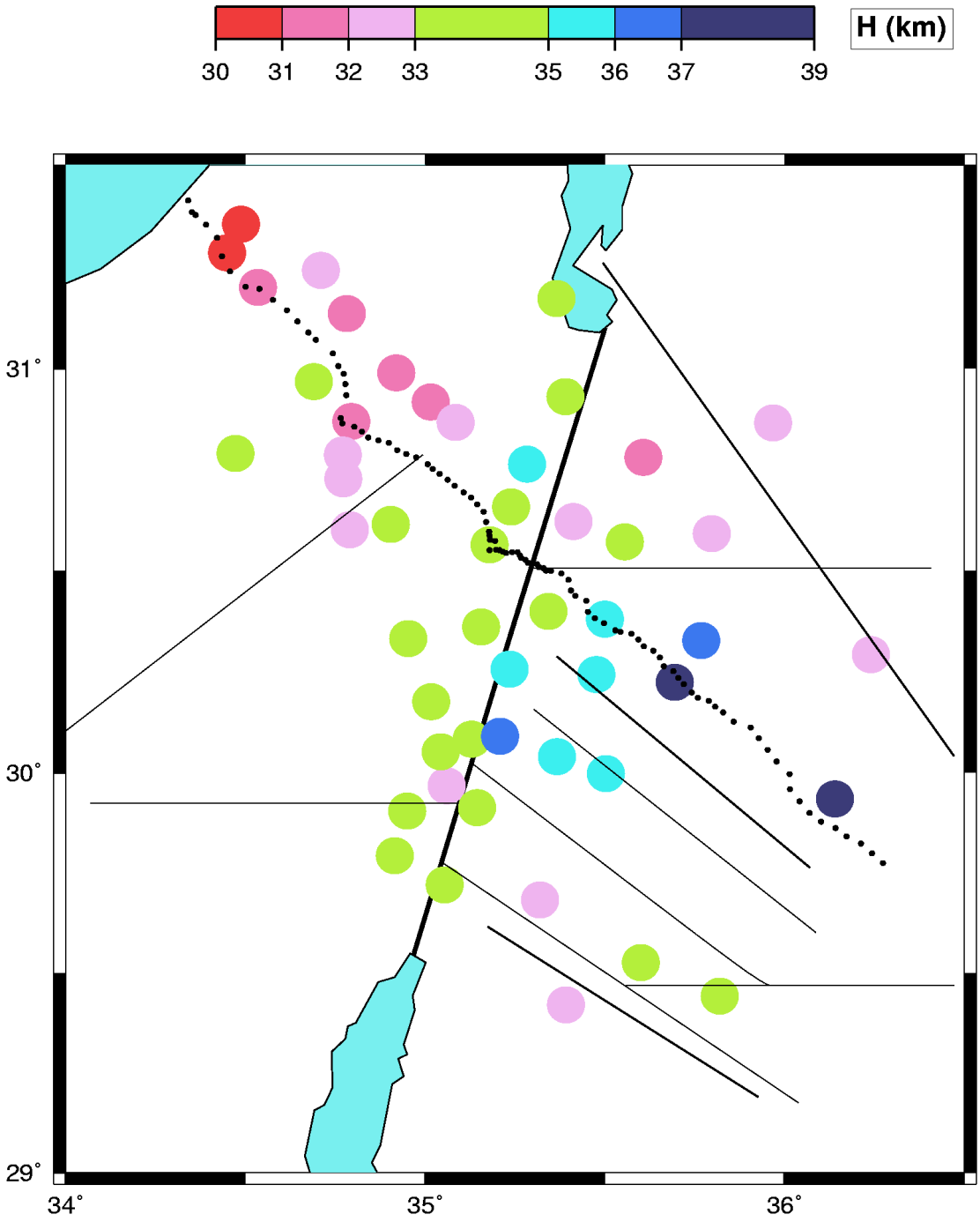

Figure (5.14): Map of the crustal thickness (H) as calculated by applying the Zhu and Kanamori method to the receiver function data. The lines indicate the faults in the investigated area.

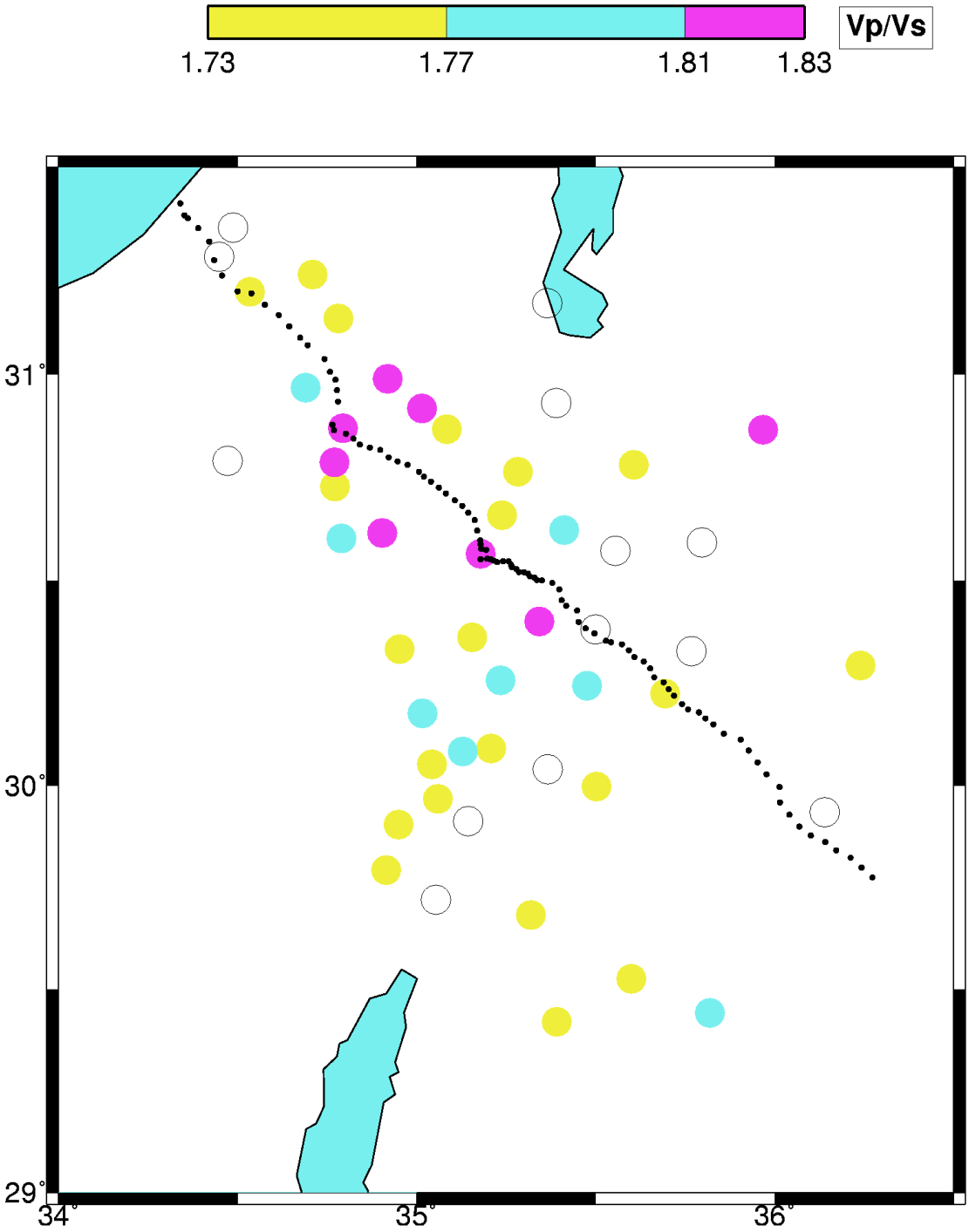

Figure (5.15): The colored circles mark the stations for which the Vp/Vs values have been determined by the Zhu and Kanamori method . Open circles represent stations for which the Vp/Vs ratio has not been determined. There is no clear systematics in the distribution of the Vp/Vs ratios. The highest Vp/Vs ratios are observed somewhat west of the DST.

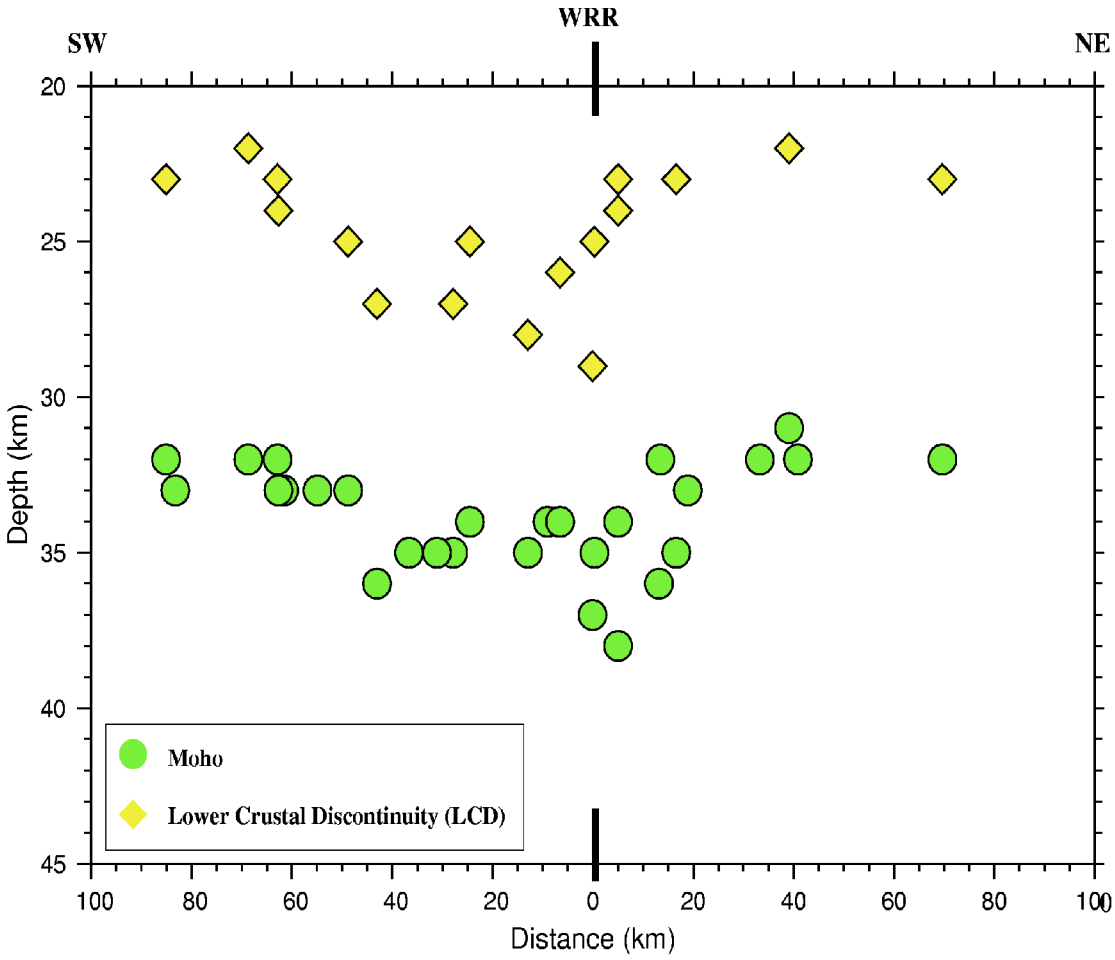

Figure (5.16): Projection of Moho depths and Lower Crustal Discontinuity (LCD) on and east of the DST on a south-west to north-east profile perpendicular to the controlled source profile. Both Moho and LCD, are unusually deep (by chance) at the location of the controlled source profile (WRR).

5.5 A Lower Crustal Discontinuity (LCD) East of the DST

In addition to the three major phases in Fig. 5.4 labeled 'sediments',' Moho' and 'Moho multiples', it is obvious that there is an additional phase between the Moho conversion and the Moho multiples. This phase is labeled LCM and interpreted as a Lower Crustal Multiple since it arrives parallel to the Moho multiples. This LCM is present on and east of the DST. This feature has been seen at 18 stations. The visual readings of the delay times for the LCM (listed in Table 3.1 Appendix C) lie in the range of 9-13 s.

Figs 5.17- 5.19 represent the results of receiver function inversion at 5 seismic stations of group B that clearly show the LCM, and at 1 seismic station of group A. The inversion method was not used as described by Kind et al. (1995) and is discussed in Section 3.2.5. Such a technique may fit the waveform nearly perfectly, but the resulting models are very complicated, often oscillatory. Instead of inversion, the forward modeling using simple models were done, in which each significant phase has been identified, although the waveform fit might not be as perfect as in the inversion. The description for 2 seismic stations in Fig. 5.17 is given in the following:

The top three panels (A, B and C) show the waveform modeling of station JW05, located on the eastern side of the DST. The last panel shows the waveforms modeling of station ID08 located on the western side of the DST.

Panel A compares the computed waveforms (continuous line) of a sedimentary layer over a granitic half space with the observed waveforms (dashed line). The computed and observed times of the conversion at the base of the sediments agrees well, the computed amplitude is, however too small. Since 3D structure plays an important role, it is not reliable to fit this amplitude into a 1D model.

In Panel B, a lower crustal discontinuity has been added, which produces a direct conversion, which has a too small amplitude compared with the observations. It also produces a multiple fitting exactly the observed phase, which is therefore interpreted as multiple of the Lower Crustal Discontinuity (LCD)

In Panel C, the Moho has been added, which fits the observed signal near 5 s, together with the lower crustal conversion very well. Also the Moho multiples fit the later parts of the signal perfectly.

In Panel D, where the crustal structure seems to be simple, the computed phases coincide well with the observed ones.

The Moho conversion in group B is indeed a superposition of a conversion from the lower crust and the Moho. The two directly converted phases cannot be separated due to their relatively long periods and small differential times, while the multiples of both phases are clearly separated.

Fig. 5.20 shows the depth position of the lower crustal discontinuity east of the DST. The values are located in the range of 21 to 29 km depth. Like in the Moho depth map in Fig. 5.16 the lower crustal discontinuity is deepest near the WRR profile except for station JS03. At the northern and southern ends of the station network the LCD is shallower again. A comparison of the depth determinations of Moho and Lower Crustal Discontinuity by the NVR, WRR profiles and receiver functions is presented in Section 5.6, Fig. 5.21.

The LCD is clearly observed in the area east of the DST. A thermo-mechanical model of the DST by Sobolev et al. (2003) shows that the crustal structure of the DST results mainly from the geologically documented 107 km left lateral displacement between the Arabian plate and the African plate placing lithospheric blocks with different crustal structures opposite each other.

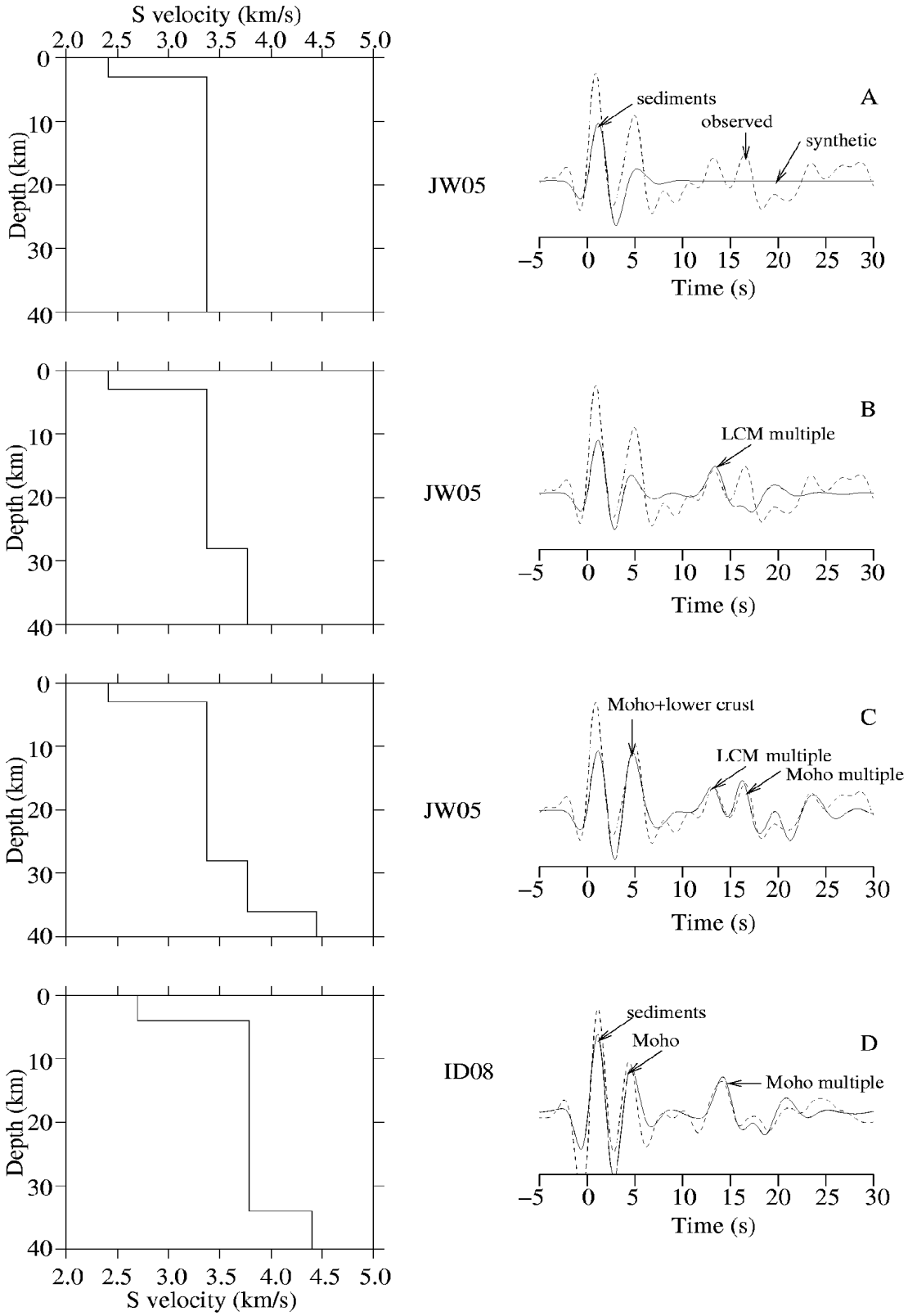

Figure (5.17): Waveform modeling of one station east (JW05) and one station west (ID08) of the DST.

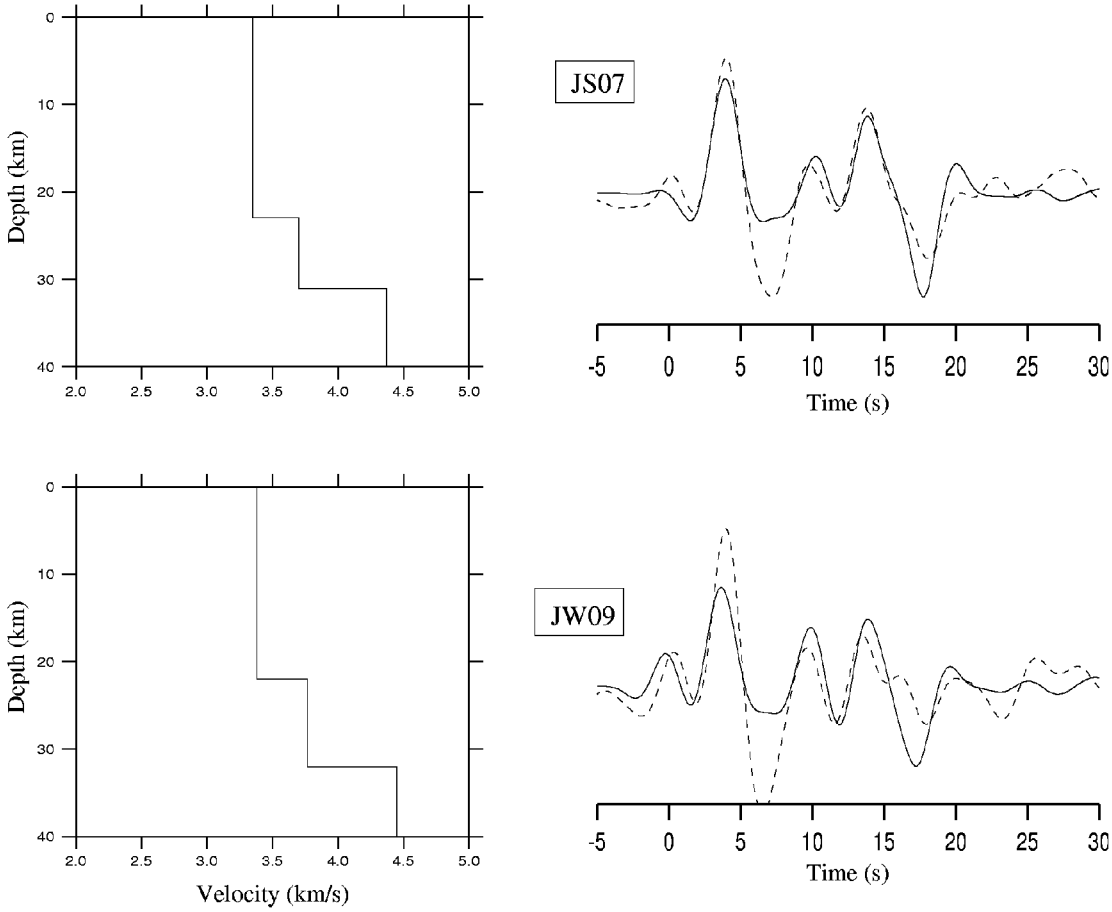

Figure (5.18): Results of forward modeling at stations JS07 (first panel) and JW09 (second panel) east of the DST. The left panels show the final model, whereas in the right panel the computed waveforms (continuous line) and the observed waveforms (dashed line) are shown. The results show Moho conversions at depths of about 32 km at both sites. The Lower Crustal Discontinuity (LCD) at 23 km and 22 km depths is also observed at both sites.

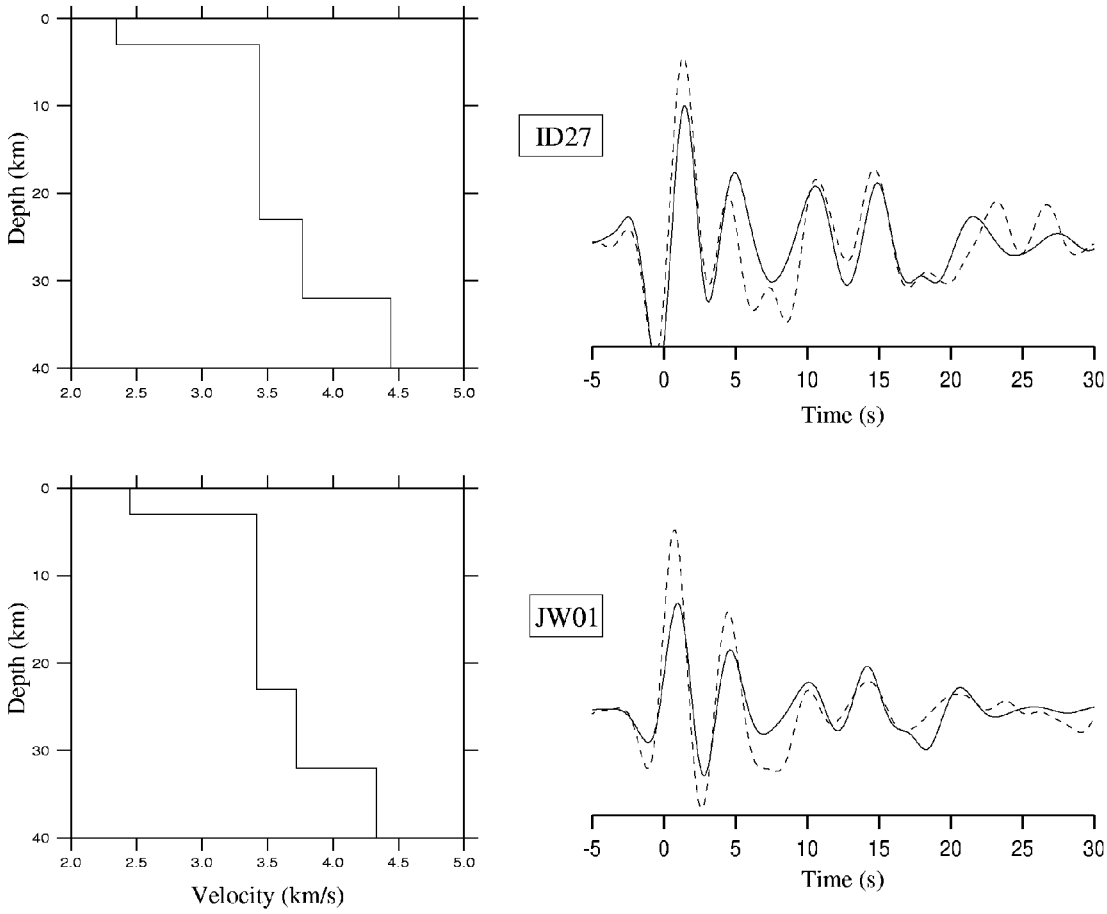

Figure (5.19): Results of forward modeling at stations ID27 located on the DST (first panel) and JW01 (second panel) east of the DST. The left panels show the final model, whereas in the right panels the computed waveforms (continuous line) and the observed waveforms (dashed line) are shown. The results show Moho conversions at 34 and 32 km depths at both sites. The Lower Crustal Discontinuity (LCD) at 24 km and 23 km depths is also observed at both sites.

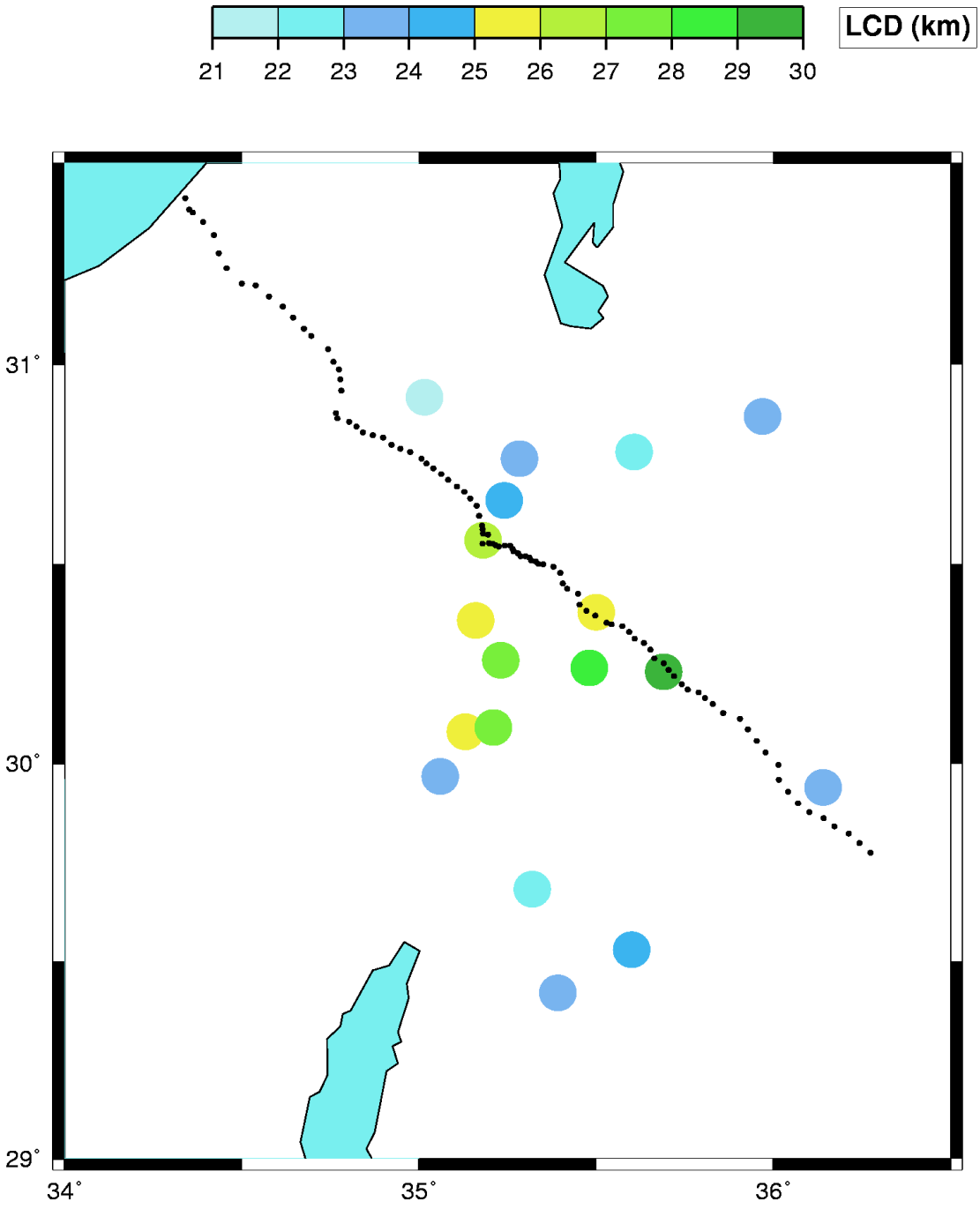

Figure (5.20): Map of the Lower Crustal Discontinuity (LCD). The LCD is deepest near the controlled source line except for station JS03. At the northern and southern ends of the station network the LCD is shallower again.

5.6 Comparison of Results from DESERT and other Geophysical Studies

As mentioned in Chapter 1, the DESERT project consists of several geophysical experiments in addition to the passive component (DESERT Group, 2000). One of them was a 260 km long wide-angle profile from the Mediterranean to the highlands in Jordan, coinciding with a 100 km long steep angle reflection profile across the DST.

The wide-angle data show a continuous increase of the crustal thickness from 27 km at the coast that agrees with an earlier study of Makris et al. (1983), to about 41km under the Jordan highlands. The general trend of a continuous Moho depth increase is confirmed by the results of the near vertical reflection profile.

Receiver function results show the same trend of an increasing Moho depth along the WRR profile. West of the DST, the Moho deepens from 30 km to about 35 km beneath the DST and continues to deepen to nearly 40 km at the eastern most stations. The continuous deepening from west to east is observed along the entire controlled source profile.

Fig. 5.21 compares the depth determinations of the Moho and the lower crustal discontinuity by steep and wide-angle controlled source techniques and receiver functions along the 100 km long steep angle reflection profile across the DST. The results from all techniques yield the same picture of the crustal thickness. East of the DST the receiver function results indicate a shallower Moho in the north and south than along the controlled source profile (see Fig. 5.16).

Fig. 5.16 projects the depths of the Moho and the lower crustal discontinuity (LCD) on and east of the DST on a southeast to northwest profile perpendicular to the controlled source line (WRR). The Moho in the north and south of the controlled source line east of the DST seems to have similar depths like west of the DST. This means that the continuous deepening of the Moho from west to east across the DST is only a local feature, and does not exist everywhere east of the DST.

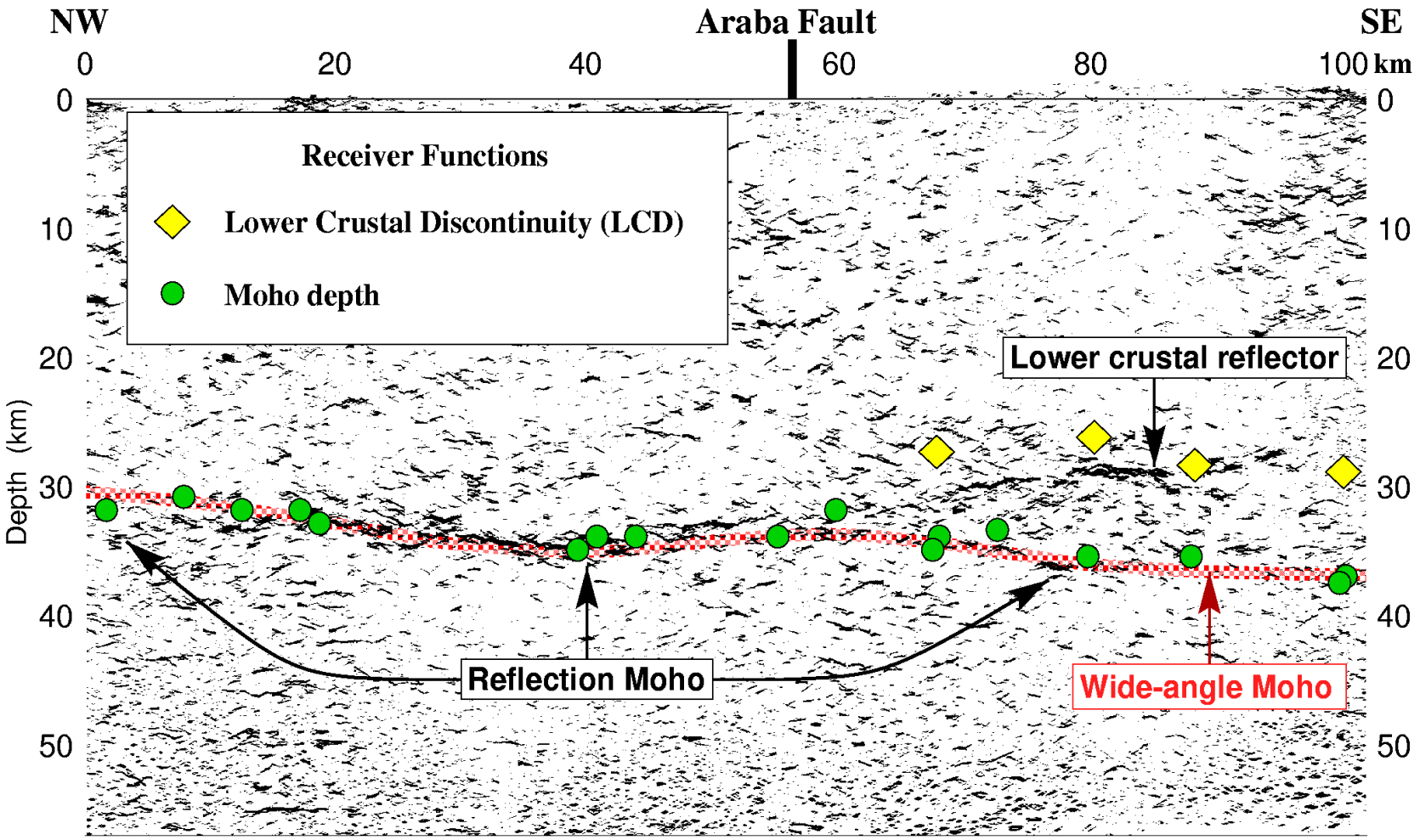

Figure (5.21) : Comparison of depth determinations of Moho and LCD by steep and wide angle controlled source techniques (DESERT Group, 2003) and receiver functions.

A lower crustal reflector was observed from the NVR data, rising from the Moho at the DST to less than 30 km depth towards the East (Fig. 5.21) . The same feature is observed also from receiver function results on the DST and to the eastern side of it within the same depth range obtained by controlled source data. No similar feature is observed west of the DST (Fig. 5.21). The lower crustal discontinuity and as well as the Moho are deep at the location of the controlled source profile (WRR) and shallow in the north and south (Fig. 5.16).

The refraction studies of Ginzburg et al. (1979a,b, 1981); Ginzburg and Folkman (1980); El-Isa et al. (1987) and the reflection study of Yuval and Rotstein (1987) report a crustal thickness not less than 32 km in the Aqaba region. The crustal thickness of about 33 km obtained from receiver function analysis is in good agreement with the results of the above-mentioned studies. The 32-35 km crustal thickness obtained from receiver functions beneath the DST is also in a good agreement with the results obtained from travel time modeling for earthquakes by El-Isa (1990).

Based on teleseismic receiver functions, Hofstetter and Bock (2003) report a crustal thickness of 33-35 km underneath station EIL. They also report a crustal thickness of 34 ± 2 km at HITJ station that agrees with earlier studies of El-Isa et al. (1987a,b) and Rodgers et al. (1999). Underneath station BGIO, a crustal thickness of 32 ± 2 and 33 km was obtained by Hofstetter and Bock (2003) and Sandvol et al. (1998), respectively. (see Fig. 4.1 for the location of the three permanent broadband stations).

5.7 Upper Mantle Discontinuities

Using the complete dataset of teleseismic events recorded at epicentral distances between 30°-93°, receiver functions were calculated to search for converted waves from the transition zone between the upper and lower mantles. The transition zone is bounded by seismic discontinuities that are globally observed at average depths of 410km and 660km.

Both discontinuities probably reflect phase transitions in the Olivine mineral of mantle rock. Indeed, all mantle minerals (Olivine, Orthopyroxene, Clinopyroxene, Garnet, Magnesiowustite and Perovskite) are solid solutions of two or more endmember components, predominantly an iron one and a magnesium one with a limited admixture of a calcium and an aluminum endmember in Perovskite (for more detail, see Helffrich, 2000). Thus, any reaction between two phases leads to a pressure-temperature region, therefore, the location of those discontinuities is temperature and pressure dependent.

The 410 km and the 660 km are the globally observed discontinuities, and the chemical reactions taking place between the 400 and 700 km depth are:

1) The 410 km discontinuity is associated with the transition from Olivine to Wadsleyite (spinel-β phase). The reaction is:

$$(Mg,Fe)2SiO4 \Rightarrow (Mg,Fe)2SiO4$$

Olivine (α) Wadsleyite (β)

2) The 660 km discontinuity is generally believed to represent the transition from ringwoodite (spinel g-phase) to a Perovskite and Magnesiowustite structure. The reaction is :

$$(Mg,Fe)2SiO4 \Rightarrow (Mg,Fe)O + (Mg,Fe)SiO3$$

The two transitions have Clapyeron slope of opposite signs such that in cold mantle regions the 410 km discontinuity is elevated and the the 660 km discontinuity is depressed yielding a wider depth range for the transition zone. In hot mantle regions the opposite effect is observed resulting in a narrower transition zone (Gossler and Kind, 1996).

However, variations in the delay time of the 410 km discontinuity are indicating changes in the average upper mantle velocity. Variations in the differential time of the two discontinuities indicate mainly thickness changes of the transition zone, which are indications of temperature variations at that depth (Li et al., 2003).

Due to the attenuation and scattering of weak converted phases that originate from the mantle discontinuities and travel through the heterogeneous upper mantle and crust, it is necessary to stack receiver functions. Before stacking, a distance moveout correction is applied using the IASP91 global reference model and a reference slowness of 6.4s/° permitting summation of records from different distances. A moving average stacking technique has been used.

Fig. 5.22 shows the signals from both discontinuities. The traces are plotted along the longitude of their piercing points at 660 km depth from west to east. The distribution of the piercing points of both discontinuities are shown in Fig. 5.23. Practically all of them are east of the DST covering the territories of Jordan.

The traces in Fig. 5.22 are summed over a window of one degree. Then the window is moved by 0.2 degrees and a new summation trace is created. Finally, all traces are summed and plotted at the top.

Measuring the travel times at the peak amplitudes of the P-to-S conversions, a value of 24.2 s is obtained from the differential time of both discontinuities. The arrival time of the 410 signal is 45.6 s. IASP91 values are 24.0 s for the differential time between both discontinuities and 44.0 s for the 410 km discontinuity. This would suggest that the upper mantle east of the DST is not typical for a continental upper mantle, indicating that the upper mantle east of the DST is warm and 3-4 % slower

than the standard model. This could mean that the upper mantle in the region is still influenced by several geodynamical processes involving rifting, uplift and magmatism above the transition zone and below the Moho as the thickness of the transition zone is close to the global average.

From shear-wave velocity structure of the Sinai sub-plate derived by receiver function analysis, Hofstetter and Bock (2003), observed that both discontinuities are late by about 2 s compared to the IASP91 model.

To study and compare the upper mantle across the DST with receiver functions, more stations should be installed further to the south (in the Sinai), since most events are arriving from the northeast.

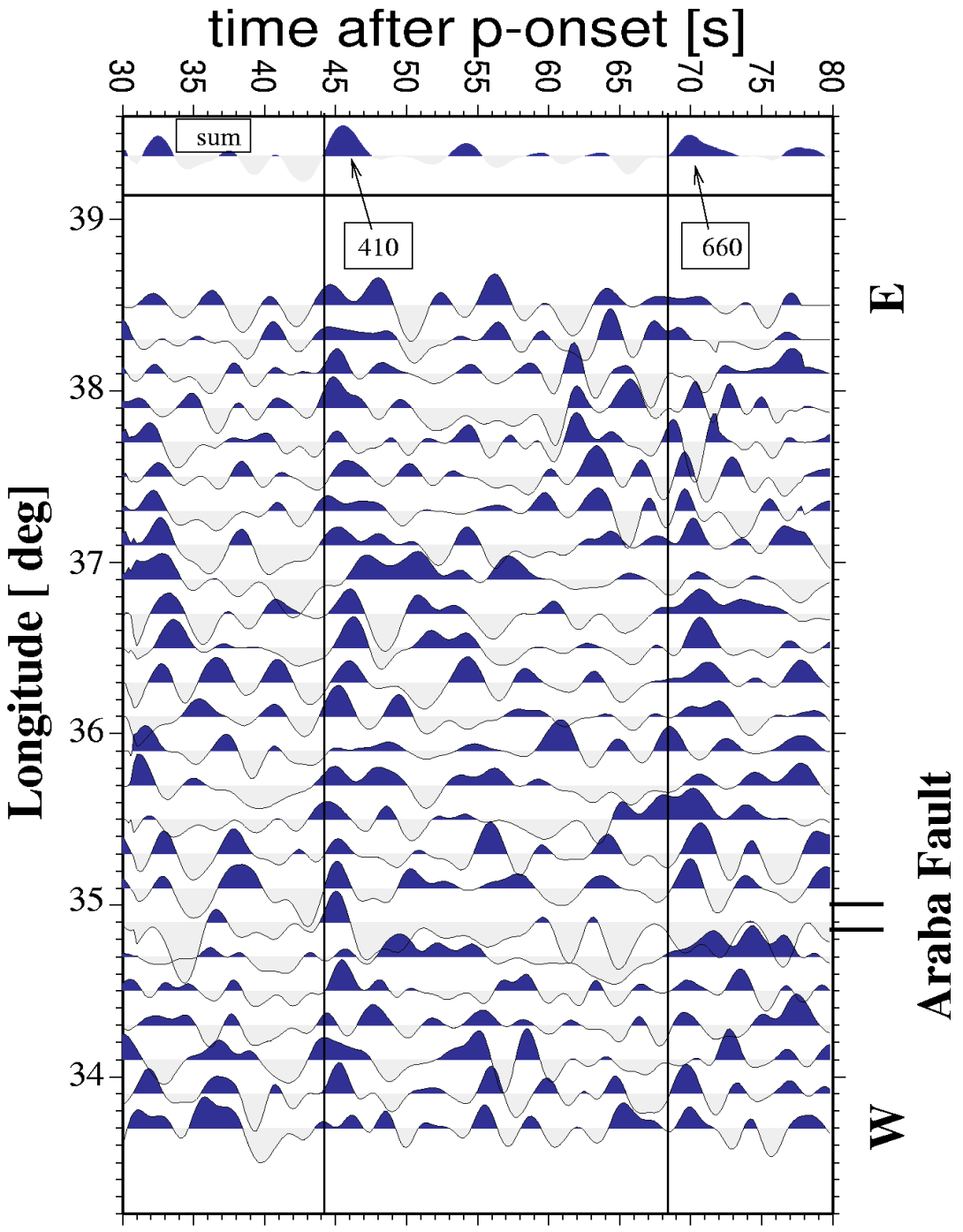

Figure (5.22): Observations of conversions from the 410 and 660 discontinuities in the DESERT experiment. The traces are plotted along the longitude of their piercing points at 660 km depth.

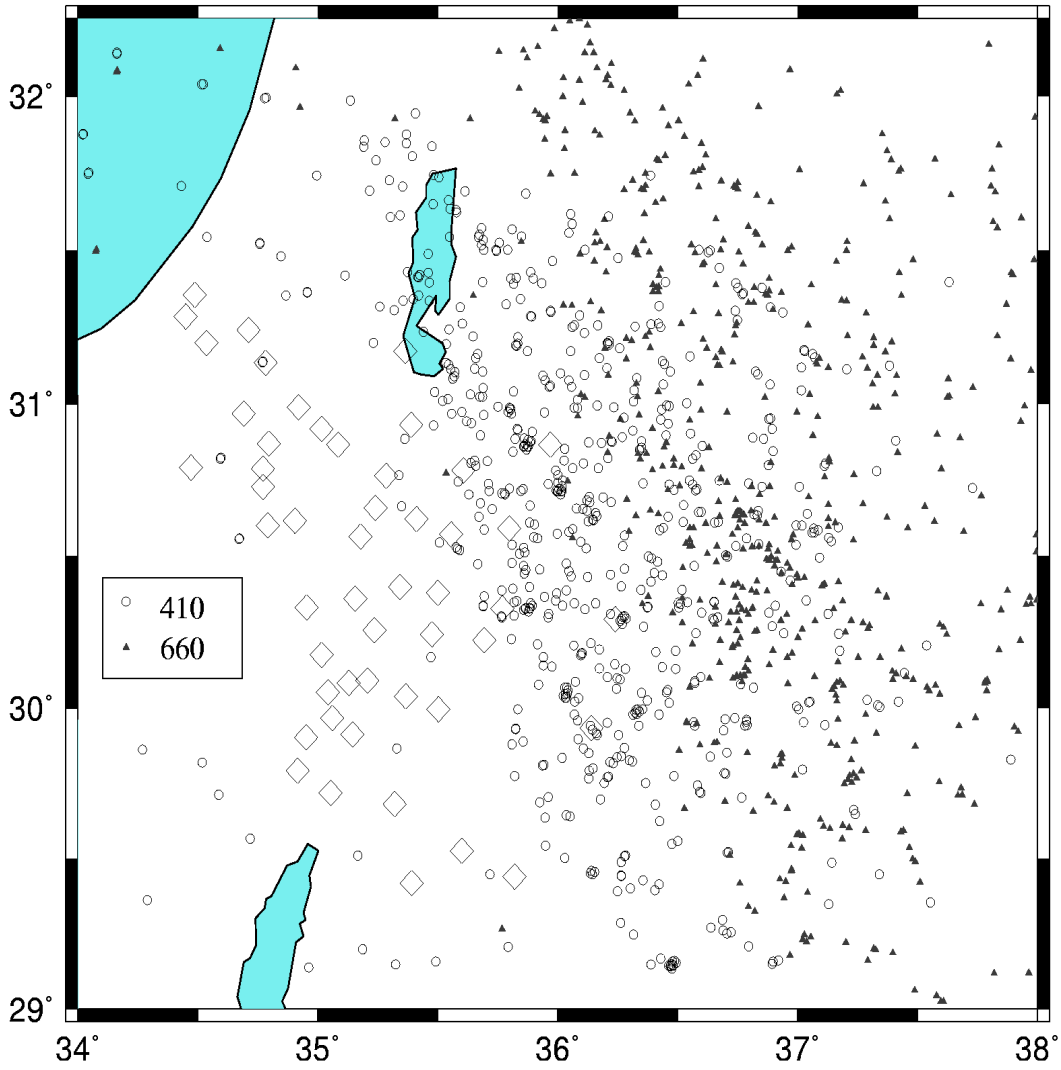

Figure (5.23): Distribution of piercing points at the 410 and 660 km discontinuities. Open diamonds are the stations. Practically all piercing points are east of the DST.